NTNU

Norwegian University of
Science and Technology

Numerical simulation of air injection in Francis turbines

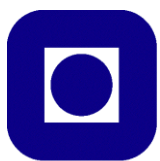## Livia-Ioana Pitorac

Livia I. Pitorac

Air Injection in Francis Turbine

Master thesis in Hydropower Development

Trondheim, June 2017

Supervisor: Michel J. Cervantes

Norwegian University of Science and Technology
Faculty of Engineering
Department of Energy and Process Engineering

NTNU
Norwegian University of
Science and Technology

Abstract

With the increasing use of renewable energy such as wind and solar, the power market operation is changing. The energy producers using classic resources have to adapt. This applies to hydropower plants as well, which are more often operated away from their best efficiency point, involving a significant increase in load variations, as well as start/stop to regulate the grid frequency. During turbine operations away from the best efficiency point and at part load, the vortex breakdown phenomenon encounters in the draft tube, which lead to the formation of a rotating vortex rope (RVR). The RVR is the result of a flow instability associated with low-frequency pressure pulsations, noise and vibration, limiting the operational range of the turbine. Various methods for RVR mitigation have been investigated for many years, but so far, none has yielded outstanding results. The most popular method for decreasing pressure pulsations is air injection. Air injection methods can be divided into passive and active.

This study focuses on setting the basis for a new active control method (varying air injection), using Computational Fluid Dynamics (CFD) modelling. Among the possible benefits of implementing pulsated air injection are, decreasing the necessary air quantity, and the mitigation or even cancelation of the pressure pulsations due to RVR.

First, a numerical model is developed for part load operation, and validated using measurements performed for the Francis-99 workshop. Next, standard air injection methods are compared, for which it is determined that the pressure amplitude associated with the RVR decreases by more than 50% when a constant air injection of 1% is applied. Finally, a possible method for determining the frequency, phase, and amplitude for varying air injection is described. It is shown that the system responds four times slower to air nozzle opening than to air nozzle closing, and that a pulsated air frequency equal to the RVR frequency is optimal. As for the air fluctuation, only a small variation is determined to be beneficial to the system (between 0.9 and 1% in this case).

iv

Acknowledgement

Table of Contents

List of Figures

x

List of Tables

Abbreviations

NTNU – Norwegian University of Science and Technology

CFD – Computational Fluid Dynamics

Re – Reynolds number

SST - Shear Stress Transport

SAS – Scale Adaptive Simulation

GGI – General Grid Interface

FVM – Finite Volume Method

UDS – Upwind Differencing Scheme

RMS – Root Mean Square

LDA – Laser Doppler Anemometry

PIV – Particle Image Velocimetry

FFT – Fast Fourier Transform

DFT – Discrete Fourier Transform

IFFT – Inversed Fast Fourier Transform

RVR – Rotating Vortex Rope

DO – Dissolved oxygen

DR – Discharge Ring

AI – Air Injection

BEP – Best Efficiency Point

PL – Part load

FL – Full load

VL – Vaneless Space

DT – Draft Tube

FT – Full Turbine

1 Introduction

1.1 Background and motivation

In recent years, since the introduction and fast growing use of renewable energy, the energy market in most countries has changed, influencing energy system dynamics and implicitly the role of hydropower in an energy system. The increasing share of energy produced from renewable sources such as wind and solar may lead to imbalances between supply and demand in energy markets. Nowadays, despite the significant development of energy storage possibilities, there are still limitations that make storing large quantities of energy impossible. Thus, during low production and high demand times, the intermittency from wind and solar needs to be counterbalanced by peaking power plants to cover the demand [1]. In this matter, hydropower is one suitable alternative, with several advantages such as the use of a renewable resource and a fast response time (start/stop time). From here it developed the need of changes in hydropower operational strategy, hydraulic turbines being more often operated away from their design point (best efficiency point), with either a reduced flow rate (part load) or a higher flow rate than the design rate (full load). However, during off-design operation, hydropower operators noticed that problems such as cavitation, severe noise and strong vibrations encountered, which likewise lead to a decrease in the turbine efficiency [2, 3, 4]. The frequency of the vibrations could not be related with any known source. Investigations showed that those frequencies encountered due to certain pressure pulsations, associated with vortex breakdown phenomenon. In hydraulic turbines, the vortex breakdown phenomenon can be observed under the form of a rotating vortex rope (RVR).

Along the years, multiple methods have been developed for mitigating the effects of the RVR, such as: the use of directional fins, redesign of the draft tube, shape modification of the runner cone tip, water injection, passive air injection, and active air injection. The air injection methods are among the most popular, providing multiple advantages: not only the control of pressure fluctuations, but also the increase in dissolved oxygen (DO) obtained through water aeration, which is very beneficial from an environmental point of view. Air can be injected in various parts of the turbine (before the runner, through the turbine shaft, through the runner blades, through a discharge ring placed in the draft tube wall, etc.), each with advantages and disadvantages [5].

As Resiga [6] pointed, the implemented method should follow the following four guidelines: first, it is important to address the excitation cause of the RVR, and not the effects; second, the

device should not affect the turbine performance in operational ranges other than the aimed ones, third, the use of air injection should not result in a decrease of the present value of the turbine efficiency; and finally, the method should be simple and robust, with a small implementation cost. As most of the old hydropower plants are close to the end of their lifetime, and therefor undergoing refurbishment, now is the optimal time to develop a solution for problems encountered during part/full load operations. This way, the overall cost of building a control system decreases significantly.

1.2   Objectives and limitations

The main objective of this thesis is to investigate and improve the existing air injection methods by means of Computational Fluid Dynamics (CFD) modelling. In order for this to be achieved, the entire work is divided into three parts. In the first part, a CFD model is developed and validated with measured data. Second, standard air injection is investigated. Finally, the effects of pulsating air injection are analyzed in comparison to standard air injection, with the purpose of researching improvements to air injection methods in order to decrease the necessary amount of injected air.

The expected limitations of the project are the time allocated for the thesis and more importantly, the limited available computational resources.

1.3   Thesis outline

This thesis is structured in seven chapters, followed by the list of references. The first chapter presents an introduction, covering the background and motivation for choosing this specific project, together with the proposed objectives and expected limitations of the thesis work.

The second chapter is a literature review, presenting useful information from the studied materials to show the present development state of air injection use for RVR mitigation.

The third chapter presents background for understanding the modelling theory. This section discusses the governing equations; turbulence models; domain interface models; compressibility; and multiphase flow theory, applied for the cases of interest. In the last part of the chapter, Fast Fourier Transform (FFT) theory is incorporated, necessary for understanding the further processed results.

Chapter 4 summarizes information about all the studied test cases, starting with the turbine description in order to give a better understanding of the model basis. The second part of the

chapter describes the computational domain, numerical model, and boundary conditions for the developed models.

In chapter 5, the results are presented and discussed, starting with the part load simulation and comparisons for model validation. Further, the results of the constant air injection cases are presented with the aim of finding the optimal air injection rate for the turbine. Finally, trials for further improvements of the optimal constant air injection case are discussed (i.e. variable air injection).

The thesis ends with a conclusion chapter and a chapter discussing the recommendations and future work, chapter 6 and chapter 7, respectively.

2 Literature review

2.1 Vortex breakdown

Pressure pulsations occur in the draft tube of a Francis turbine during off-design operation. These are associated with the vortex breakdown phenomenon, which is a flow instability characterized by a swirling flow formed of two concentric flow regions: an outer region where the fluid transport encounters and an inner region characterized by a dead core or a stagnation zone [7]. The main factor that determines the vortex breakdown phenomenon is the swirl number S_n, which, in fact, represents the non-dimensional ratio of tangential momentum to axial momentum:

$$S_n = \frac{\int_0^{R_i} c_m c_u \, r^2 \, dr}{R_i \int_0^{R_i} c_m^2 \, r \, dr} \tag{2.1}$$

where R_i is the pipe radius, c_m and c_u are the meridional (axial) and tangential velocities, and r is the location vector.
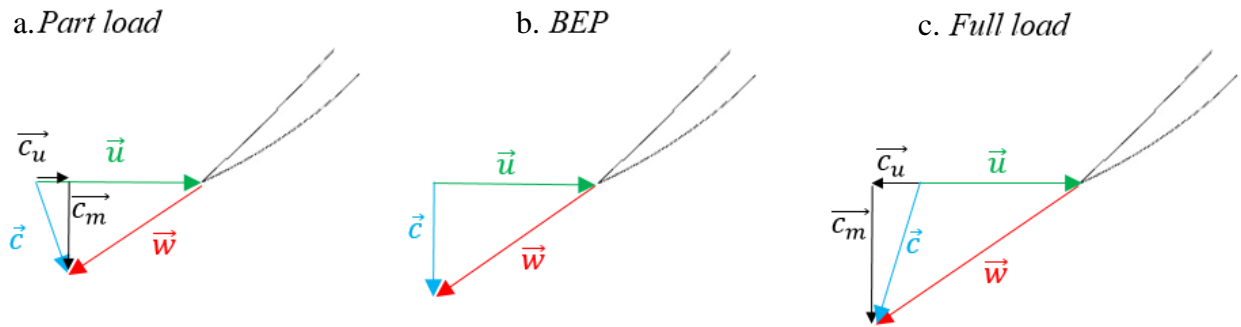
Figure 2.1 Velocity triangle at runner outlet

A Francis turbine is designed to run at a certain water discharge, generally known as best efficiency point (BEP). Around BEP, the velocity triangle at the runner outlet of a Francis turbine is characterized by a small tangential velocity (Figure 2.1.b). With deviation of turbine operation from BEP, the flow regime in the draft tube changes. As Francis turbines are single regulated turbines, the angle between the blade velocity (*u*) and the relative velocity of leaving water (*w*) cannot be adjusted by varying the flow through the turbine, thus tangential velocity

(c_u) appears, resulting in a small swirl number. As shown in Figure 2.1.a, a decrease in the flow rate (part load - PL) results in the increase of the tangential velocity, having the same direction as the runner rotation, leading to a co-rotating vortex. In Figure 2.1.c, the full load (FL) operating case, the runner rotation and the tangential velocity are in opposite directions, leading to a swirl opposite to the runner rotation.

In hydraulic turbines, for large swirl, the vortex breakdown phenomenon can encounter at the shear layer between the two zones. This generally has the shape of a rope, usually known as rotating vortex rope, surrounding the stagnation zone (Figure 2.2). Cassidy [8] showed that the stagnation zone diameter varies with the swirl number. The RVR is not fixed, but it rotates with a frequency ranging between 0.2 and 0.4 of the runner frequency [7, 9].
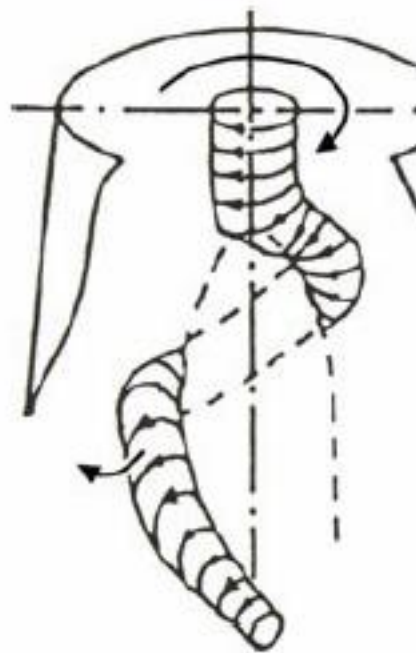
Figure 2.2 Structure of vortex breakdown in a draft tube [7]

The presence of RVR in the draft tube of a turbine induces pressure fluctuations. For understanding the roots of RVR formation, it is necessary to understand its components; according to Nishi [10], the pressure pulsations are determined by a synchronous component (plunging mode) and an asynchronous component (rotating mode). While the asynchronous component is related to flow instabilities, such as RVR [11], the synchronous component is associated with the axial velocity [12]. Goyal [13] showed that the plunging component develops before the rotating component. As pointed out by Bosioc [14], in order to differentiate

between the two components of RVR, two pressure signals p_1 and p_2 are used, measured in two points symmetrically placed with regard to the draft tube axis, and calculated as follow:

$$Plunging\ mode\ of\ the\ pressure\ signal = \frac{p_1 + p_2}{2} \qquad (2.2)$$

$$Rotating\ mode\ of\ the\ pressure\ signal = \frac{p_1 - p_2}{2} \qquad (2.3)$$

2.2 Air injection

Flow aeration in turbines can be done for a variety of purposes, among the most important being increasing the dissolved oxygen content [15, 16], decreasing the impact of cavitation on the runner [17, 18], and avoiding unsteady flow patterns and self-induced oscillations [19, 20].
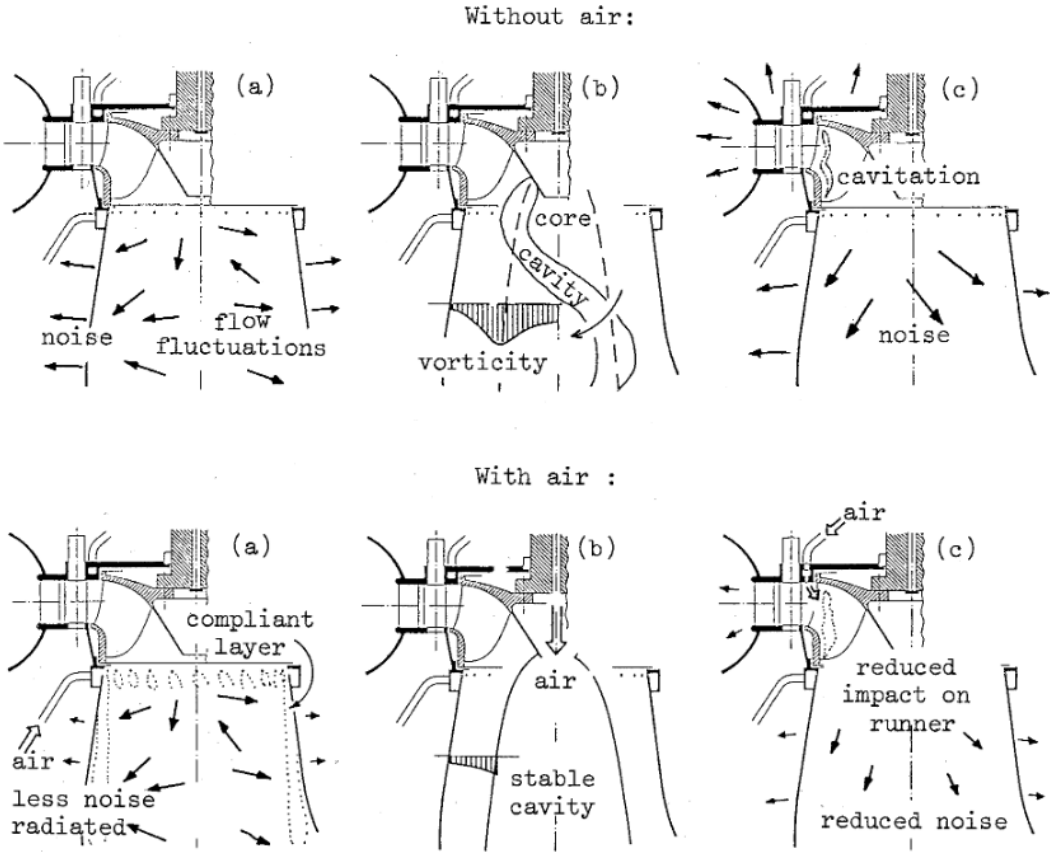
Aeration for draft tube flow noise reduction (a), suppression of the helical vortex pattern (b), and reduction of cavitation impact and noise (c).

Figure 2.3 Comparison between flow characteristics in draft tube with and without air injected [5]

7

By introducing air in water, the low-pressure flow regions are filled with air cavities, increasing the flow compressibility, which leads to a reduction of the flow noise, as show in Figure 2.3 .a. Figure 2.3.b. shows that air cavities introduced in a swirling flow lead to stability in the core region, reducing or even eliminating a flow regime that favors the development of vortex breakdown. [5] By filling the low pressure cavities with air, instead of vapor as usually occurs naturally, an instantaneous collapse of the vapor bubbles is avoided, thus less noise and erosion encounter, as shown in Figure 2.3.c.

Depending on the objective of using aeration, various methods can be implemented, the main ones presented in Figure 2.4. Two of the most investigated aeration methods are peripheral aeration (DR-discharge ring aeration) and central aeration, considered the most effective for RVR mitigation [5]. The DR method tends to counteract the effects of the RVR, and does not affect its formation source as does central aeration. This is contrary to one of the four characteristics of a good aeration method that Resiga described in [6] (see Background and motivation chapter). Furthermore, the central aeration method was proved the most effective during part load [21], which is the case of interest in this project.
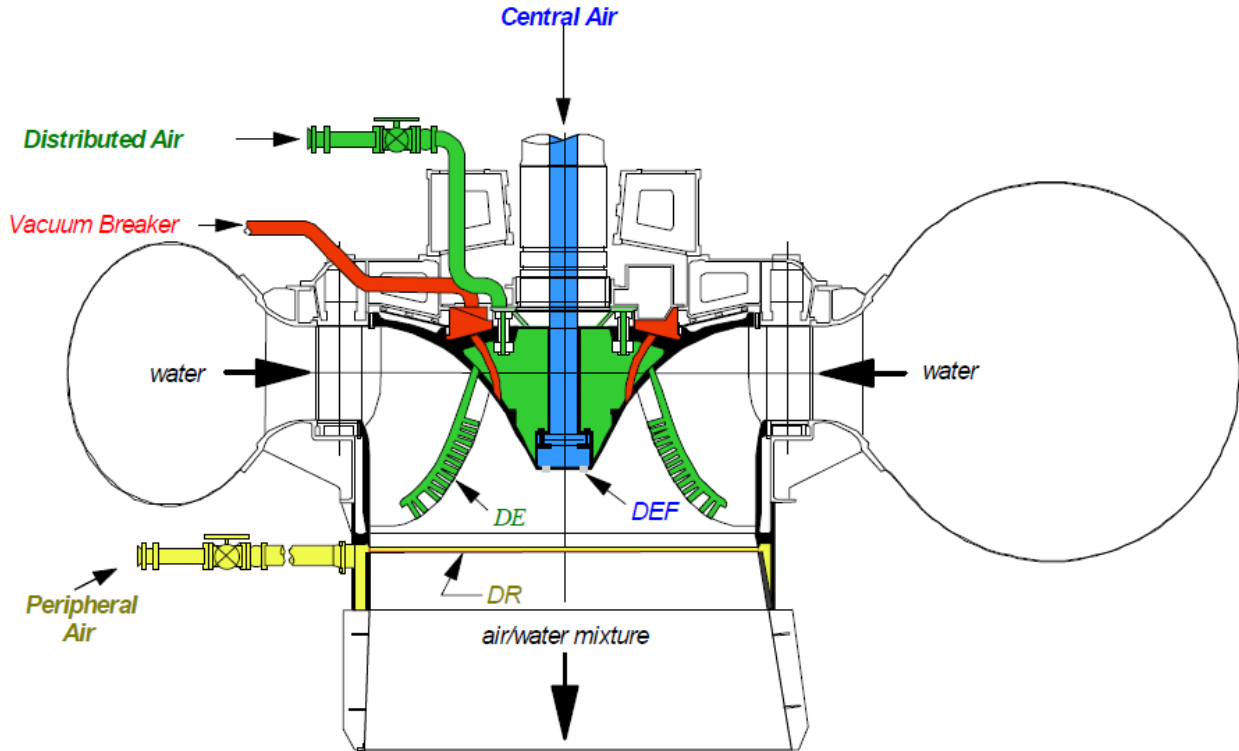
Figure 2.4 Aeration methods in Francis turbine [16]

In draft tubes, atmospheric air can be admitted due to negative pressure (self-venting, passive design) or compressed air can be injected (active design), which is actually needed in turbines with high submergence or with a high tail water. The latter method additionally allows better control of the system, which is of interest in most cases.

Little has been discusses about the physics behind the effect of air in mitigating the pressure pulsations induced by the RVR, but it has been attributed by some to the decrease in water hammer pressure, due to the lower speed of sounds in bubbly liquid [18].

Air introduced in the center of a draft tube first increases the pressure in the cavity, which influences the entire flow regime. This has a similar effect to lowering the tail water level [5]. When injected under the runner, it leads to reduction of the pressure pulsations and cavitation by changing the hydroacoustic characteristics, which causes a change in the frequencies and amplitudes [22]. The air flow rate (Q_{air}) is calculated as shown in equation (2.4), where φ represents the imposed rate for the injected air, and Q_{water} is the water flow rate.

$$Q_{air} = \frac{\varphi \cdot Q_{water}}{100} \qquad (2.4)$$

Not much information regarding the proper diameter of the air injection nozzle was found. Only in Foroutan [23], nozzle diameter ranges are calculated for water injection, ranging between 10 and 50% of the runner cone.

In order to produce the optimal effect air injection, the proper amount of air has to be determined. The recommended amount of injected air varies between 0.06% [5] to 4% [24] of the water flow rate. The injection of air after the runner results in an increase in pressure in the draft tube. The turbine efficiency decreases with the increase in air flow rate, which limits the range of air flow rate to maximum 3% [25]. In addition to mitigating the RVR, the air injection system should not decrease the overall turbine efficiency, meaning that the air injection system should be adaptable for various operation points, and ideally closed during BEP operations [14].

3 Modelling Theory

3.1 Governing equations

Numerical modelling in ANSYS CFX is done based on solving a set of unsteady Navier-Stokes equations, which describe the relationship between the pressure p, temperature T, and density ρ of a fluid. The Navier-Stokes equations govern the fluid motion, representing the conservation of momentum. In equation (3.1), the first term represents the inertial forces, while the next three represent the pressure forces, viscous forces, and external forces (source of momentum S_M) applied to the fluid respectively.

$$\underbrace{\rho\left(\frac{\partial u}{\partial t} + u \cdot \nabla u\right)}_{inrtial\ forces} = \underbrace{-\nabla p}_{pressure\ forces} + \underbrace{\nabla \cdot \tau}_{viscous\ forces} + \underbrace{S_M}_{external\ forces} \tag{3.1}$$

where the relation between the stress tensor (τ) and the strain rate (μ) is:

$$\tau = \mu\left(\nabla u + (\nabla t)^T - \frac{2}{3}(\nabla \cdot u)I\right) \tag{3.2}$$

The Navier-Stokes equations are always solved together with the continuity equation (3.3), which represents the mass conservation equation.

$$\frac{\partial \rho}{\partial t} + \nabla \cdot (\rho u) = 0 \tag{3.3}$$

For flow in a rotating frame with a constant angular velocity, S_M has to include the effect of centrifugal forces ($S_{centrifugal}$) and Coriolis forces ($S_{coriolis}$) [26].

$$S_M = S_{centrifugal} + S_{Coriolis} \tag{3.4}$$

$$S_{centrifugal} = -\rho\ \omega \times (\omega \times r) \tag{3.5}$$

$$S_{Coriolis} = -2\rho\ \omega \times u \tag{3.6}$$

where u is the relative frame velocity, ω is the angular speed, and r is the location vector [26].

3.2 Turbulence model

Turbulence is described by a Reynolds number (Re) higher than 4000, meaning that it occurs when the inertial forces are more significant in a flow compared to the viscous forces. In Computational Fluid Dynamics, the most commonly used turbulence models are k-ε and k-ω Shear Stress Transport (SST), due to the reduced numerical effort and the good computational accuracy. These models are part of the two-equation eddy viscosity turbulence models, and are characterized by solving separate transport equations for the turbulent kinetic energy (k) and for the dissipation (ε and ω). In addition to the two governing equations, the SST model needs a wall-scale equation to be solved, which makes it slightly more resource consuming. Both these models have a lack of exact transport equations, which comes from the fact that ε describes the dissipative scale, and not the large scale. As the scope of two-equation turbulence models is to determine the influence of large-scale motion on mean flow, they need to be modeled with an additional equation for k [26]. A solution for this matter comes from implementing the SAS-SST model, with the following transport equations:

$$\frac{\partial \rho k}{\partial t} + \frac{\partial}{\partial x_i}(\rho u_i k) = G_k - \rho c_\mu k \omega + \frac{\partial}{\partial x_j}\left[\left(\mu + \frac{\mu_t}{\sigma_k}\right)\frac{\partial k}{\partial x_j}\right] \tag{3.7}$$

$$\frac{\partial \rho \omega}{\partial t} + \frac{\partial}{\partial x_i}(\rho u_i \omega) = \alpha \frac{\omega}{k} G_k - \rho \beta \omega^2 + Q_{SAS} + \frac{\partial}{\partial x_i}\left[\left(\mu + \frac{\mu_t}{\sigma_\omega}\right)\frac{\partial \omega}{\partial x_j}\right] + (1 + F_1)\frac{2\rho}{\sigma_{\omega,2}}\frac{1}{\omega}\frac{\partial k}{\partial x_j}\frac{\partial \omega}{\partial x_j} \tag{3.8}$$

The SAS-SST model differs from the SST model by the Q_{SAS} source term. A more detailed description of the SSA-SST model can be found in [27].

Implementing one of the two eddy viscosity models is a bit controversial for modelling the part load, some considering the k-ε more appropriate [28], and others the SST [29, 30]. Furthermore, as shown in [31], for part load operations, results determined using eddy viscosity models are more inaccurate than the ones obtained with more complex models.

3.3 Domain interface model

Domain interfaces represent the way of connecting domains or matching meshes. They have a wide range of use including: connecting repeating flow fields where boundaries have a rotation or translation periodic, connecting non-matching grids, connecting domains stationary domains with frame changing domain as rotor-stator interfaces. In ANSYS CFX, there are three interface

12

models: translational periodicity, rotational periodicity and general connection. As shown in Figure 3.1, the periodic interface allows modeling simplified geometry by reducing the model to a passage, such as a single blade passage in a rotating machine.
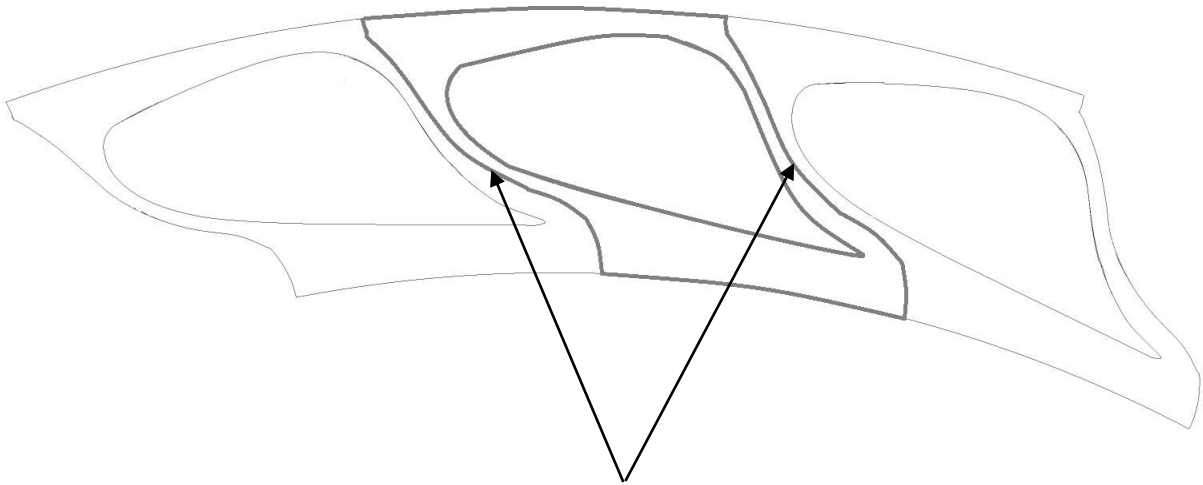
Figure 3.1 Periodic interfaces

In ANSYS CFX, the General Connection interface model is characterized by three frame change/mixing models: frozen rotor, stage (mixing-plane), and transient rotor-stator.

In the frozen rotor analysis, the flow is modeled from one component to the next one by moving the reference frame while the relative position of the components is maintained fixed. It has the advantage low consumption computational resources, but it may yield wrong physics for local flow values because the transient effects at the frame change are not accounted for.

The stage (mixing-plane) model averages the fluxes through multiple bands on the interface circumference, treating each fluid zone with a steady state approach. The data from adjoining zones are implemented as averaged boundary conditions mixed at the interface. The model works best when the circumferential variation of the flow field in a zone is not significantly changing relative to the component pitch. When considering the computational effort, the stage model requires more time for convergence than the frozen rotor model, but less than the transient rotor-stator model. It is recommended to start implementing the mixing-plane model based on an approximate solution generated using the frozen rotor model.

Figure 3.2 Axial (top) and radial (bottom) rotor-stator illustration (schematic illustration of the mixing plane concept) [26]

In Figure 3.2, a schematic illustration of the mixing plane concept is presented for an axial rotor-stator interface and a radial rotor-stator interface. In both cases, there is a static domain and a rotating domain with a predefined angular velocity. The two schematics are mutually correct, regardless of the flow direction.
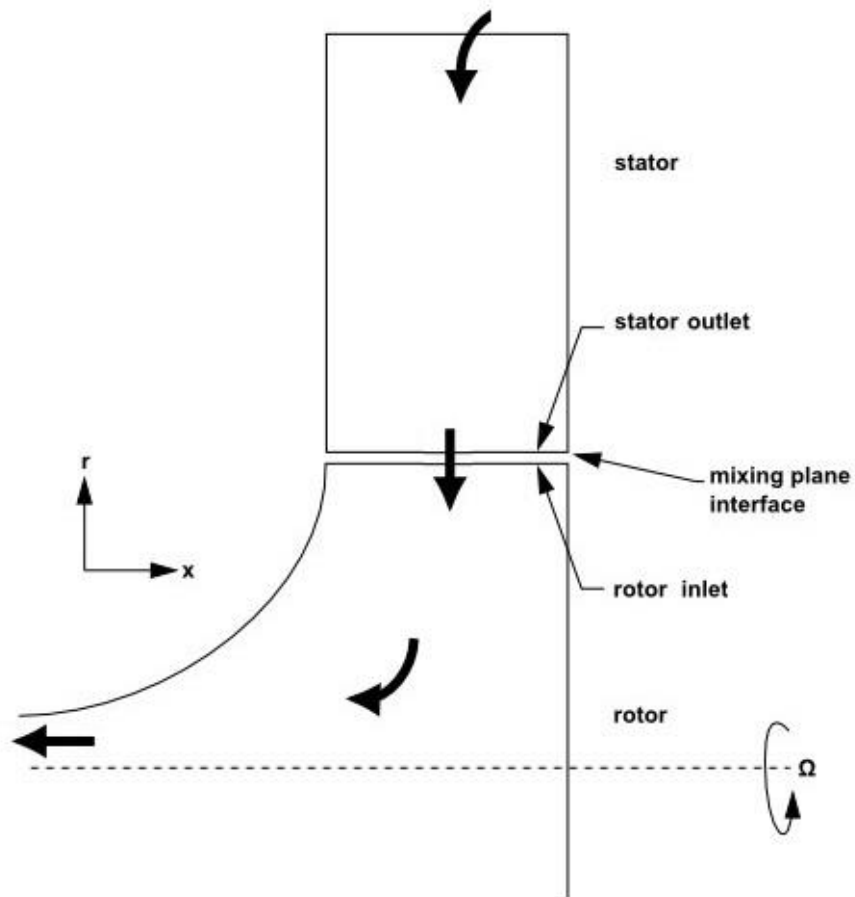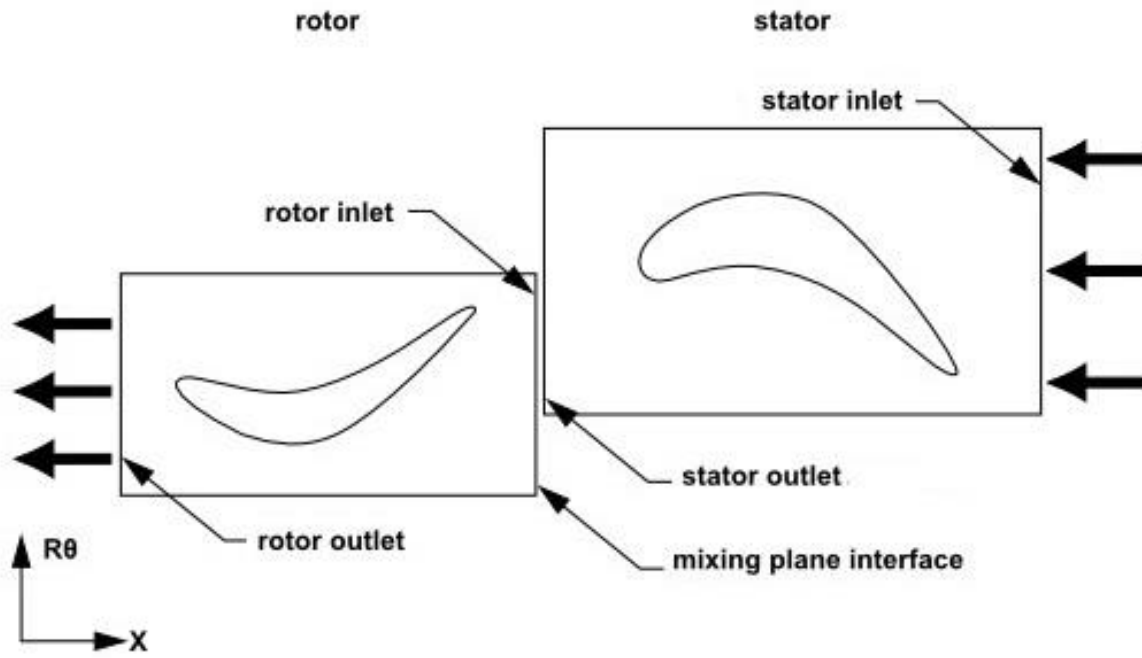
Transient rotor-stator interface model accounts for the real transient interaction between two domains, simulating the transient relative interaction between components on both sides. In this model, the position of the mesh is updated at each timestep, using a GGI connection approach between the rotational domain and the stationary domain. Because implementing the transient rotor-stator model is computationally expensive, it is recommended to start the computation from an existing prediction, obtained from a steady state solution implemented with frozen rotor, in order to decrease the necessary transient cycles for convergence.

3.4 Compressibility

Compressible fluids are characterized by the variation of their density (ρ) with pressure (p) and temperature (T) (3.9). In fluid mechanics, it is defined as the volume change of a material with pressure (3.10).

$$\rho = \rho(p, T) \tag{3.9}$$

$$\beta = \frac{1}{\rho}\frac{d\rho}{dp} \tag{3.10}$$

From the bulk modulus (k_f) (3.11), which is the inverse of compressibility (β), the density of a compressible fluid is deduced (3.12), where the subscript 0 represents the properties of the fluid at 25°C and atmospheric pressure.

$$k_f = \frac{1}{\beta} \tag{3.11}$$

$$\rho = \rho_0 \Big/ \left(1 - \frac{p - p_0}{k_f}\right) \tag{3.12.}$$

3.5 Multiphase flow

A multiphase flow represents a simultaneous flow on two or more phases with different physical or chemical properties. It can be formed by combinations of gas, liquid and solid materials under a turbulent flow. The most common multiphase flows are liquid-liquid, liquid-solid, gas-solid, gas-liquid, and three-phase flow [32]. In hydropower plants, the most common multiphase flows encountered are liquid-solid (in sedimentation problems) and gas-liquid (such as entrapped air). The flow pattern of a multiphase flow can be described as separated, mixed or dispersed components (Figure 3.3).
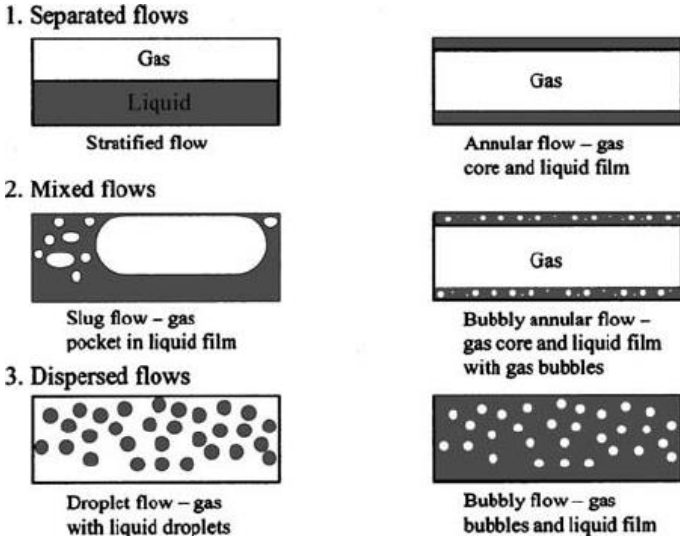
Figure 3.3 Multiphase flow patterns [33]

There are two approaches for modeling multiphase flow, namely the Euler-Lagrange approach and the Euler-Euler approach. In the Euler-Lagrange approach, the flow is modeled as a dispersed phase scattered in a continuous phase (Lagrangian phase dispersed in Eulerian phase). The particle tracking method is realized through the eyes of an observer that moves with an individual particle and determines its parameters at each spatial and temporal position. In this approach, the Navier-Stokes equations are solved for the continuous phase (3.13 and 3.14), and coupled with the Newtonian motion equations solved for the Lagrangian phase (3.15 and 3.16) through a volume conservation equation (3.17).

$$\frac{\partial}{\partial t}(r_\alpha \rho_\alpha) + \nabla(r_\alpha \rho_\alpha u_\alpha) = S_M + \Gamma_\alpha \tag{3.13}$$

$$\frac{\partial}{\partial t}(r_\alpha \rho_\alpha u_\alpha) + \nabla(r_\alpha \rho_\alpha u_\alpha u_\alpha) = -r_\alpha \nabla p + \nabla \cdot \tau_\alpha + r_\alpha \rho_\alpha g + s_\beta \tag{3.14}$$

where subscripts α and β are for the continuous phase and dispersed phase, respectively, S_M is the specific mass source, Γ_α is mass source per unit volume for mass transfer into the continuous phase, p is static pressure, τ_α is stress tensor, $\rho_\alpha g$ is gravitational force, s_β is the momentum source, and r is the volume fraction.

$$m_p \frac{dU_p}{dt} = F \tag{3.15}$$

$$F = F_D + F_B + F_R + F_{VM} + F_P + F_{BA} \tag{3.16}$$

where subscript p is for the particle and F represents the sum of forces that act on the particle: F_D - drag force, F_B - buoyancy force, F_R - centripetal and Coriolis forces, F_{VM} - virtual mass force, F_P - pressure gradient force, F_{BA} - Basset force.

$$\sum_{\alpha=1}^{n} r_\alpha = 1 \tag{3.17}$$

In the Euler-Euler approach, the flow is modeled as two continuous phases, being determined by analyzing the properties of the flow in time at a fixed point in space. In this approach, the mass conservation equation (3.18) and the momentum equation (3.19) are solved for each phase, and coupled through shared pressure and interpenetrating exchange coefficients [34]

$$\frac{\partial}{\partial t}(r_\alpha \rho_\alpha) + \nabla(r_\alpha \rho_\alpha u) = S_M \tag{3.18}$$

$$\frac{\partial}{\partial t}(r_\alpha \rho_\alpha u_\alpha) + \nabla(r_\alpha \rho_\alpha u_\alpha u_\alpha) = -r_\alpha \nabla p + r_\alpha \rho_\alpha g + F \tag{3.19}$$

where S_M refers to the mass transferred between phases, u is the mean velocity, p is the static pressure, $\rho_\alpha g$ is the gravitational force, F is the external body force.

3.6   Spatial and temporal discretization

ANSYS CFX uses a Finite Volume Method (FVM) for spatial discretization, meaning that a mesh is used for creating finite volume elements. For each formed volume, a cell-average solution of relevant quantities such as mass, momentum, and energy is conserved. In the FVM, the conservation equations for mass and momentum are integrated over each control volume [26].

There are several advection schemes available in ANSYS CFX, such as upwind, high resolution, specific blend factor, and central difference. The advection term is calculated as:

$$\varphi_{ip} = \varphi_{up} + \beta \nabla \varphi \cdot \Delta \vec{r}$$

(3.20)

Where, φ is the calculated variable, β is a parameter, φ_{up} is the value in the upwind node and $\vec{r}$ is the vector from the upwind node to node ip. The second term on the right side is called Numerical Advection Correction, and it defines the different advection schemes by the choice of β and $\nabla \varphi$.

While the first order Upwind Differencing Scheme (UDS), defined by a value of β of 0, is very robust, the discretization errors introduced with UDS are reduced in the Specific Blend Factor. However, dispersion discretization errors may be introduced, leading to non-physical oscillations. The Central Difference Scheme is characterized by a β value of 1 and $\nabla \varphi$ defined by the local element gradient. It is, however, not recommended with models other than the LES turbulence model, as it may encounter decoupling issues. In the High Resolution scheme, a nonlinear β as close to 1 (second-order-accurate) is computed, using the values from the upwind node for evaluating the advective flux, as explained in the ANSYS CFX Theory Guide [26].

The time discretization is defined by the transient scheme, presenting several options in ANSYS CFX: First Order Backward Euler, Second Order Backward Euler and High Resolution. The First Order Backward Euler scheme is similar to the Upwind Differencing Scheme for advection terms, presenting similar numerical diffusion. The Second Order Backward Euler scheme is a time-stepping scheme where the transient scheme is First Order for turbulence equations and Second Order for volume fraction. In the High Resolution scheme, the First Order Backward and Second Order Backward schemes are interchanged in order to maintain a bounded solution. [35]

3.7   Mesh theory

The need for a mesh comes from the difficulty of obtaining an analytical solution for the governing equations, unless implemented in simple cases. Thus, in order for the domain to be analyzed, it is split in smaller subdomains in which the equations can be solved. The quality of the mesh is very important for a model, as a large number of elements gives more accurate results, but the computational time increases; on the other hand, with too small a number of elements, the model tends to miscalculate the response of the analyzed system or even results in convergence failure. One important aspect to consider when building a mesh is the position of the first node. This is calculated based on a parameter y^+, the kinematic viscosity v and the friction velocity u_τ.

$$y = \frac{y^+ * v}{u_\tau}$$

(3.21)

where the friction velocity is:

$$u_\tau = \sqrt{\frac{\tau}{\rho}}$$

(3.22)

with the wall shear stress:

$$\tau = \frac{1}{2} * C_f * \rho * u^2$$

(3.23)

and the skin factor:

(3.24)

$$C_f = [2 * log_{10} Re - 0.65]^{-2.3}$$

When it comes to the mesh quality, the parameters checked by ANSYS CFX cannot be verified in ANSYS ICEM CFD, but some related parameters such as aspect ratio, angle, maximum dihedral angle and volume change are checked. For a good mesh quality, the minimum internal angle for each element must be larger than 20, and a maximum dihedral angle should be under 170. In addition, while an aspect ratio with a value of 1 corresponds to a perfectly regular element, an acceptable value for the volume change is under 2. An aspect ratio under 1000 is

required by ANSYS CFX, but accurate results are generated for values up to 10000. A detailed description of each parameter can be found in [36].

3.8   Fast Fourier Transform

The Fast Fourier Transform (FFT) is an algorithm that interprets time sequence series by computing its Discrete Fourier Transform (DFT) or its Inversed Fast Fourier Transform (IFFT). A Fourier Transform takes any time-dependent series and rearranges it in equivalent summed sinusoids by creating a representation in frequency domain. In order to obtain a consistent FFT, the signal has to be sampled at equal consecutive timesteps. Assuming that N is the number of samples, and Δt is the timestep, then the lowest frequency that FFT can compute is:

$$f_{min} = \frac{1}{N\Delta t}$$

(3.25)

The highest frequency that FFT computes is:

$$f_{max} = \frac{N/2}{N\Delta t}$$

(3.26)

The FFT algorithm can be implemented both in ANSYS CFD-Post and in MATLAB.

4 Test case

4.1 Turbine description

The test rig located at Water Power Laboratory at NTNU is a 1:5.1 scaled model based on one of the Francis turbines from Tokke power plant, in Norway. The turbine, Figure 4.1, has 14 stay vanes (SV), 28 guide vanes (GV) and 30 runner blades (15 full-length blades and 15 splitter blades).
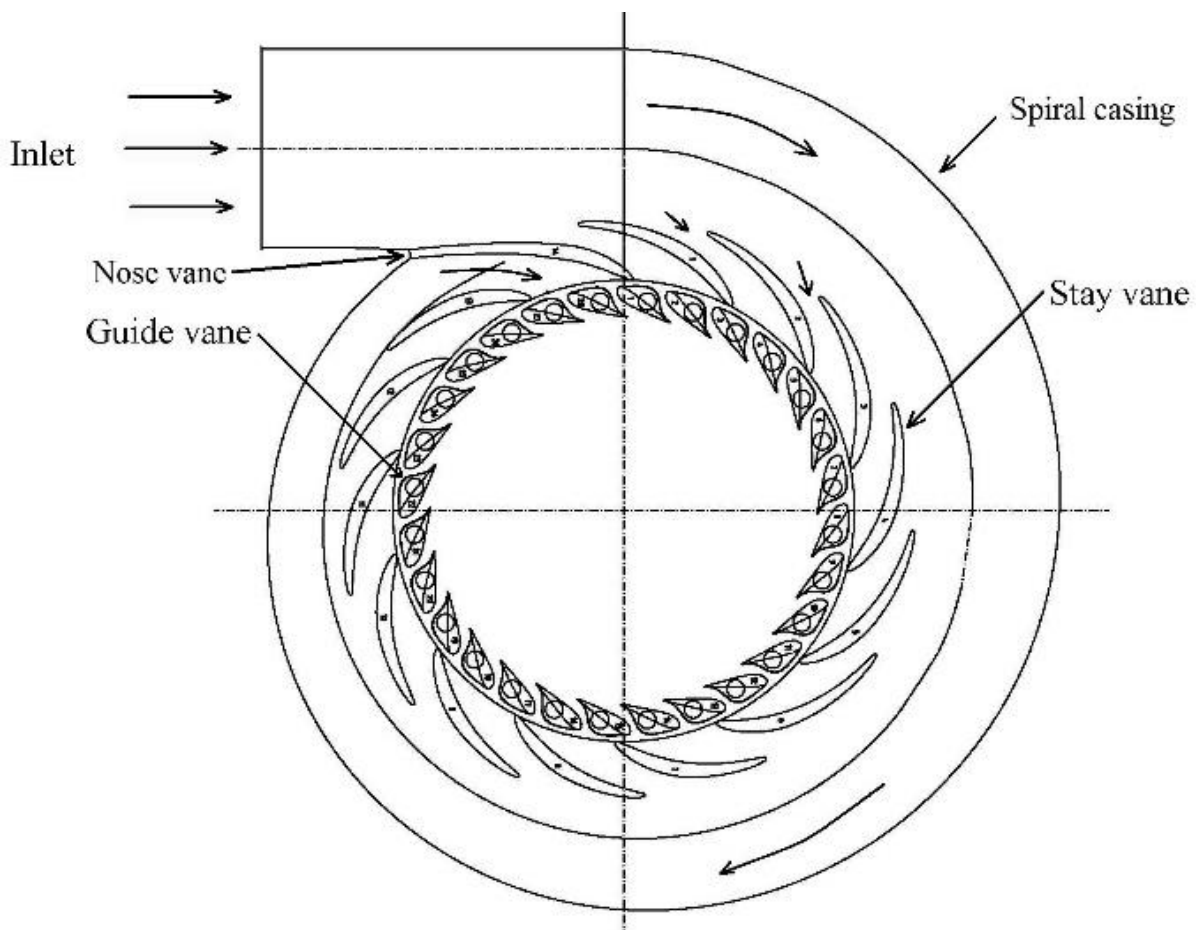

Figure 4.1 Cross section of the Tokke turbine [37]

For the Francis 99 second workshop, measurements were performed at three operating points, corresponding to Best Efficiency Point (BEP), Part Load (PL) and Full Load (FL). At PL, a for guide vane angle of 6.72° and a runner angular speed of 332.84 RPM, the flow presented the following parameters [37]:
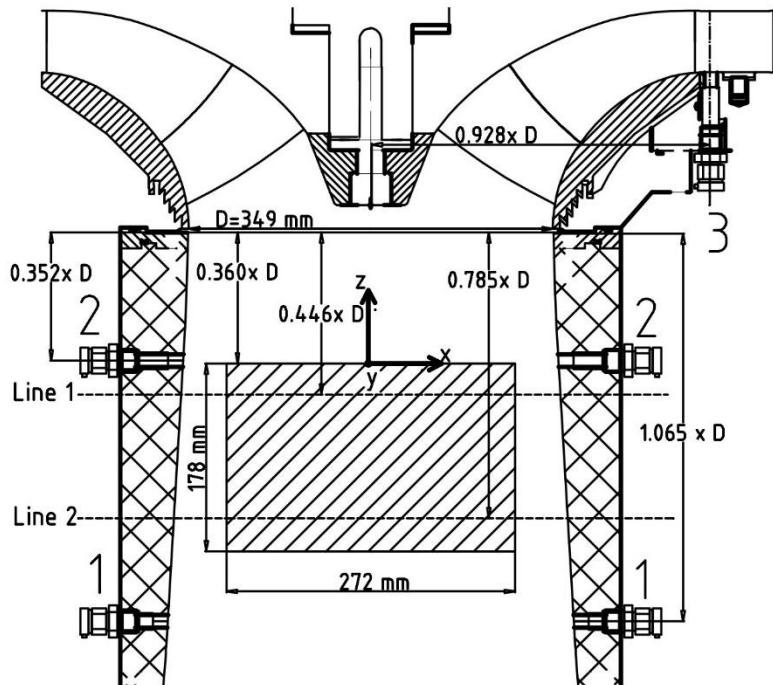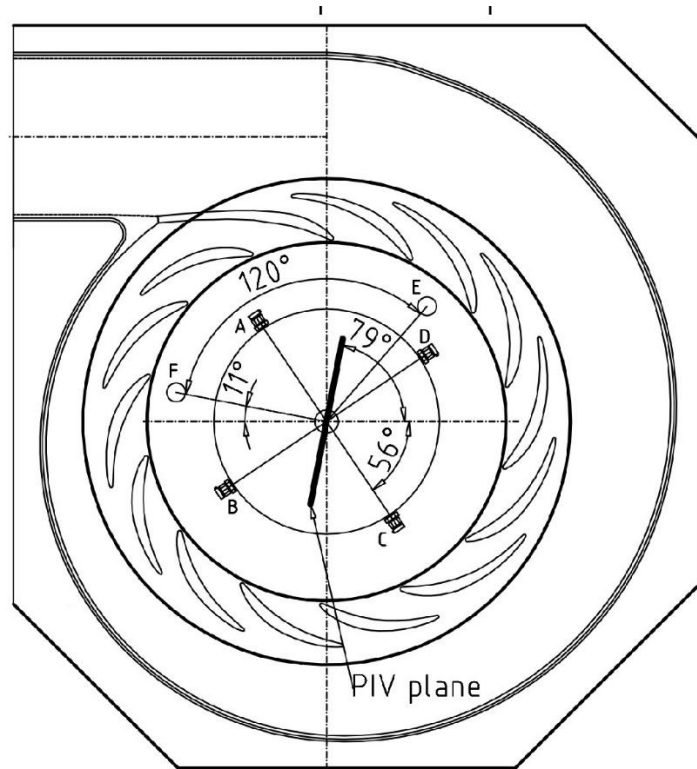
Figure 4.2 PIV measurement section in the draft tube cone (non-scaled dimensions) [34]

Pressure sensors were placed in 3 points as follows: VL2 – located in the vaneless space between the guide vanes and the runner, DT5 and DT6 – located in the draft tube cone, placed symmetrically with regard to the turbine axis. Axial and tangential velocities were measured using LDA and 2D PIV on three lines: L1 and L2 - horizontally placed in the draft tube cone,

and L3 along the turbine axis in the center of the draft tube center. Figure 4.2 shows a graphical description of measurement points locations, and more details about the turbine and the measurements can be found in [37].

Table 4.1 Flow parameters during part load measurements during Francis 99 workshop

Parameter	Part load conditions
Net head [m]	11.87
Discharge [m^3/s]	0.13962
Spiral case inlet pressure [kPa]	218.08
Draft tube outlet pressure [kPa]	113.17

4.2   Computational domain

A computational domain corresponding to the Francis turbine characteristics presented before is shown in Figure 4.3.a. This is formed of four domains: the spiral case and stay vanes (gray) having 3.43 million elements, the guide vanes (red) with 7.88 million elements, the runner (green) with 10.78 million elements, and the draft tube (blue) with 0.91 million elements.

As the runner and the guide vane domains have the highest number of elements, a decrease of the computational domains is implemented as shown in Figure 4.3.b. The spiral case and guide vane domains are reduced to a single domain (stator) with 0.83 million elements, formed of one stay vane and two guide vanes (red), and runner domain is reduced to a single passage, formed of one runner blade and one splitter (green), with 0.72 million elements.

As shown in Figure 4.3.c, a third case is developed due to the need of accurate simulation of the flow pattern at the runner outlet. Thus, the stator domain is unchanged from the previous case, while a full runner domain is implemented, leading to a 15-times increase of the runner domain elements (10.78 million elements).

Because running a full runner simulation is computationally expensive, a fourth case is analyzed, consisting of just the draft tube (Figure 4.3.d), and thus a reduction of 93.4% of the computational domain is obtained.

These cases are further referred as:

FT1 Case – full turbine with spiral case and full runner;
FT2 Case – full turbine with one stay vane, two guide vanes, and one runner passage;

FT3 Case – full turbine with one stay vane, two guide vanes and full runner;
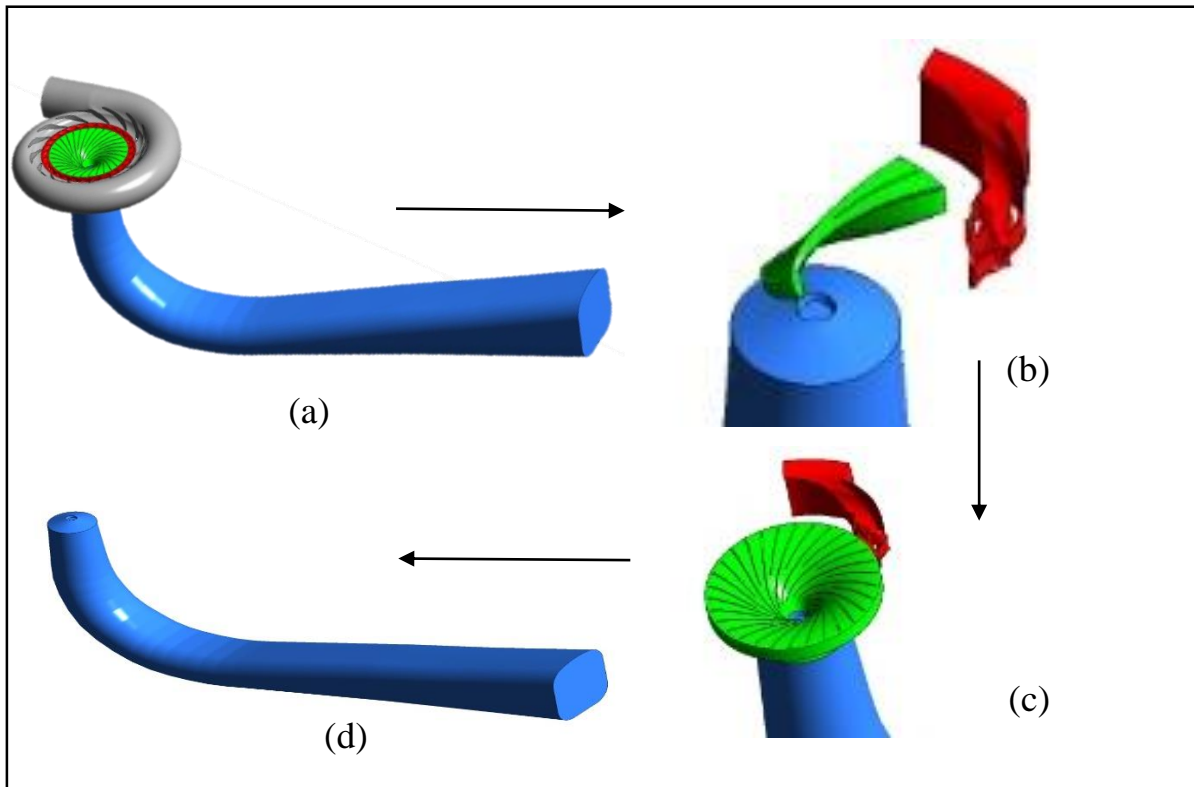
DT only Case – draft tube only.

Figure 4.3 Domain development stages

The mesh for the previously presented part load cases is provided by the Francis 99 organizers, and no additional check of the mesh quality is done. For the air injection case, the draft tube mesh is modified by implementing a nozzle boundary for the air injection, which leads to an increase from 890 880 to 894 464 million elements of the draft tube domain. For this, a mesh quality check is done, and as observed in Table 4.2, the values for the analyzed parameters are within the recommended limits.

Table 4.2 Mesh quality parameters

Mesh quality parameter	Provided mesh	Modified mesh	Recommended
Aspect ratio	1-98.3	1-98.7	<1000
Angle	36-89.55	29-89.55	>20
Maximum dihedral angle	90.4-156	90.4-165	<170
Volume change	0.99-3.9	0.99-4.5	<20

4.3   Numerical model

At first, the simulation is run for five seconds, equivalent to the total time from the measurements, but is increased to 10 seconds as suggested by Minakov [31], because a stable RVR is needed throughout the entire analyzed time series. A timestep equivalent to 5° of runner rotation was imposed, as determined by Wilhelm [38] to lead to a good convergence. In DT only case, a sensitivity analysis is performed to determine the effects of a 2° timestep on the model convergence, and to check to what extent it improves the simulation convergence.

As initial conditions, results from steady state simulations are used in all the part load cases, with simplified configurations. A k-ε turbulence model is implemented in the steady state simulations. The turbulence model during transient simulation in the FT1 case is k-ω SST, changed in FT2 case to an SAS SST model, in order to improve the accuracy of the results, and maintained the same in the following cases (FT3 and DT only).

In the air injection cases, the air-water multiphase flow is modeled using an Euler Lagrange approach, water being the continuous phase, and air being the dispersed phase with a mean diameter of 1mm. The flow is modeled as homogeneous [24], with an SAS SST turbulence model.

The simulation time control is maintained similar in the air injection cases, but the initial flow conditions are interpolated from the DT only case. Because the part load case simulation is modeled as a single-phase flow, initial air parameters have to be separately defined in the AI model, thus no air velocity and zero volume fraction conditions are defined.

For all cases, the convergence criteria is an RMS of 10e-5, with a maximum of 1000 iterations for the steady state, and RMS of 10e-4, with minimum three and maximum 10 coefficient loops in the transient simulations. A double precision run is imposed with a high-resolution scheme, which allows the flow solver to switch between the first and second order backward, based on the flow parameters.

In all simulations, monitor points are defined in the domain, equivalent to the locations of the pressure and velocity measurement points, in order to verify that the numerical models are physically correct (see [37] for exact location of the monitor points).

4.4   Boundary conditions

In the FT1 case, the boundary condition at the spiral case inlet is set as a mass flow rate of 139.62 kg/s. In FT2 and FT3 cases, the inlet at the stator has flow direction described by

cylindrical components, corresponding to an incidence angle of 9°, the attack angle of the stay vanes.

In the DT only case, the inlet boundary condition is changed to cylindrical velocity components, obtained at the rotor-draft tube interface in FT3 case, this being the most accurate simulated numerical model (see Table 5.1).

As shown in Figure 4.4, the runner cone tip is part of the draft tube domain, which is modeled as rotating wall, with the same angular velocity of 332.84 RPM as the runner domain.
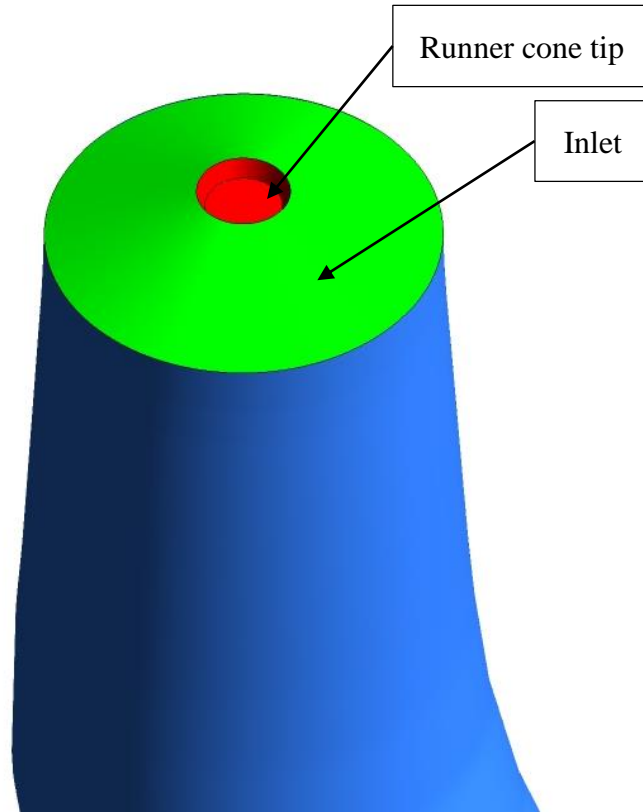

Figure 4.4 Inlet boundary for DT only case

In all simulated cases, the walls are modeled as no slip wall. The boundary condition for the outlet is opening pressure in all cases. The location of the outlet in the numerical model does not correspond to the location of the outlet pressure measurements, thus the pressure is adjusted using the Bernoulli and continuity equations, neglecting the linear losses between the two sections:

$$p_1 = p_2 + \rho g(h_2 - h_1) + \frac{\rho Q^2}{2}\left(\frac{1}{A_2^2} - \frac{1}{A_1^2}\right) \tag{4.1}$$

where subscripts 1, 2 correspond to outlet locations in the measurements and numerical model respectively, p is the pressure, ρ is the water density, g is the gravitational acceleration, h is the vertical position of a section, Q is the discharge, and A is the area of a cross section.

In the steady state simulations, the interface between the stationary domain and the runner is set as frozen rotor and the interface between the runner and the draft tube is modeled as stage mixing plane. These are changed to stage interface and transient rotor stator interface, respectively, in the transient simulations in order to achieve an accurate result in the FT1 to FT3 simulations.
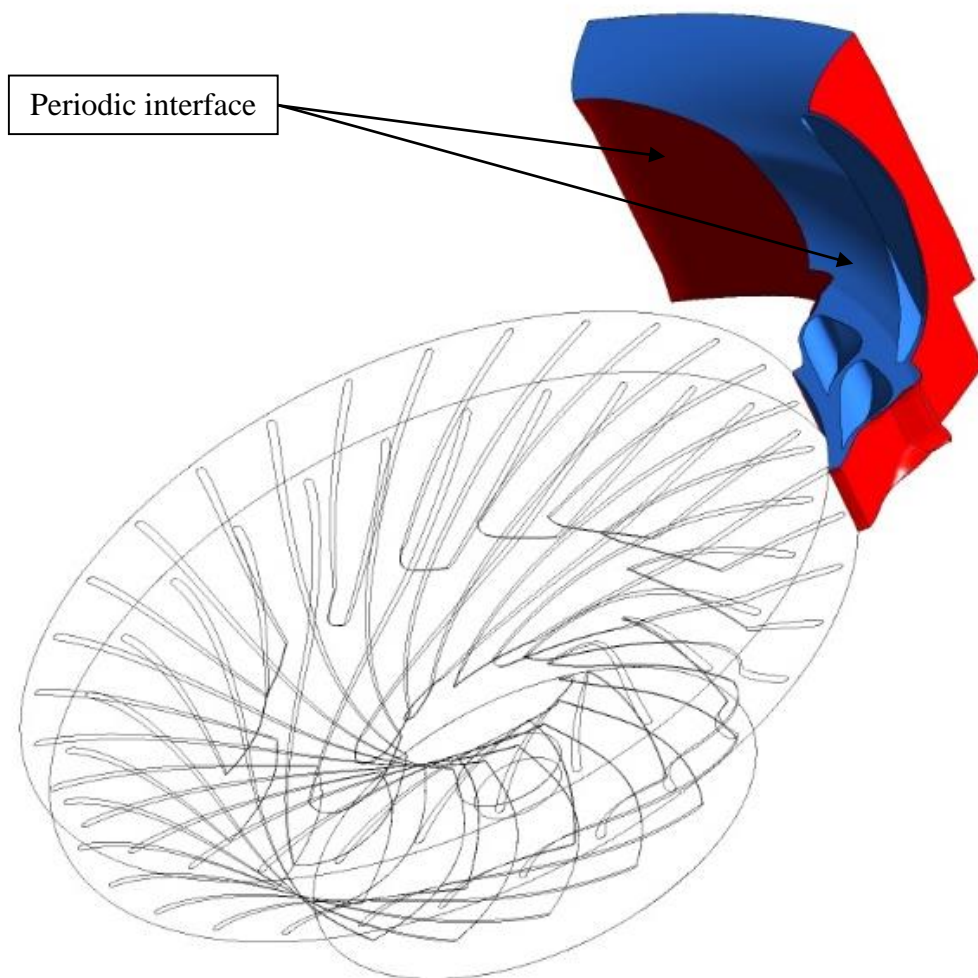

Figure 4.5 Periodic interface in stator domain

The air injection simulations were divided into two parts: constant air injection and variable air injection. In the constant AI cases, the nozzle boundary condition is set as mass flow inlet, with air flow rates equivalent to 0.5%, 1%, 2% and 3% of the water flow rate, in order to cover the

entire air flow rate range suggested in the literature. For the variable AI cases, the air is injected based on a sinusoidal curve, described in equation (4.2).

$$Q = \frac{Q_0}{2} \cdot (1 + \cos \omega t) \qquad (4.2)$$

$$\omega = 2\pi f \qquad (4.3)$$

where Q is the air flow rate at a certain timestep, Q_0 is the optimal constant air flow rate, ω is the angular frequency, t is the current timestep and f is the RVR frequency.

5 Results and discussions

5.1 Part load simulation

In this section, a brief discussion of the full turbine cases is presented along with measurements. Afterwards, an analysis is presented for the DT only case in order to determine its accuracy for simulating the flow pattern during part load.

The measurements performed for the Francis-99 project are used for validating the full turbine cases and selecting the most accurate for further investigation. At first, general parameters are compared, these being: inlet pressure, head and torque. As the inlet location in the numerical model differs from the one in the experiments, the pressure from the simulation is recalculated using the Bernoulli equation (4.1).

Table 5.1 Analyzed parameters for numerical model validation

Parameter	Measurements	FT1 case		FT2 case		FT3 case	
		Value	Error [%]	Value	Error [%]	Value	Error [%]
Pressure inlet [kPa]	219.81	237.52	8.06	235.94	7.34	233.96	6.62
Total head [m]	11.87	12.18	2.69	12.13	2.19	11.81	0.51
Torque [Nm]	420.79	472.26	14.61	470.23	11.74	460.80	9.51

As can be observed from Table 5.1, the pressure at inlet and the torque are overestimated in all cases, while the simulated head has a small approximation error. The FT3 case provides the most accurate simulation in comparison to the measurements, thus the results in this case are presented and discussed. Further analysis of the results at the monitor points for pressure and velocity are performed, i.e. a pressure frequency analysis and an axial velocity profiles analysis. Figure 5.1 presents an FFT analysis for the pressure at point VL2, which has dominant frequency around $30f_n$, corresponding to the runner blade frequency. The dominating frequency observed in the draft tube is $0.28f_n$, for both DT5 and DT6 (Figure 5.2). This frequency is attributed to the RVR, as it lies in the 0.2-$0.4f_n$ range, which is the RVR frequency domain observed by many researchers [3, 23]. All the frequencies from the simulation are similar to the ones from the measured data ($0.32f_n$ at DT5 and DT6, and $30f_n$ at VL2).
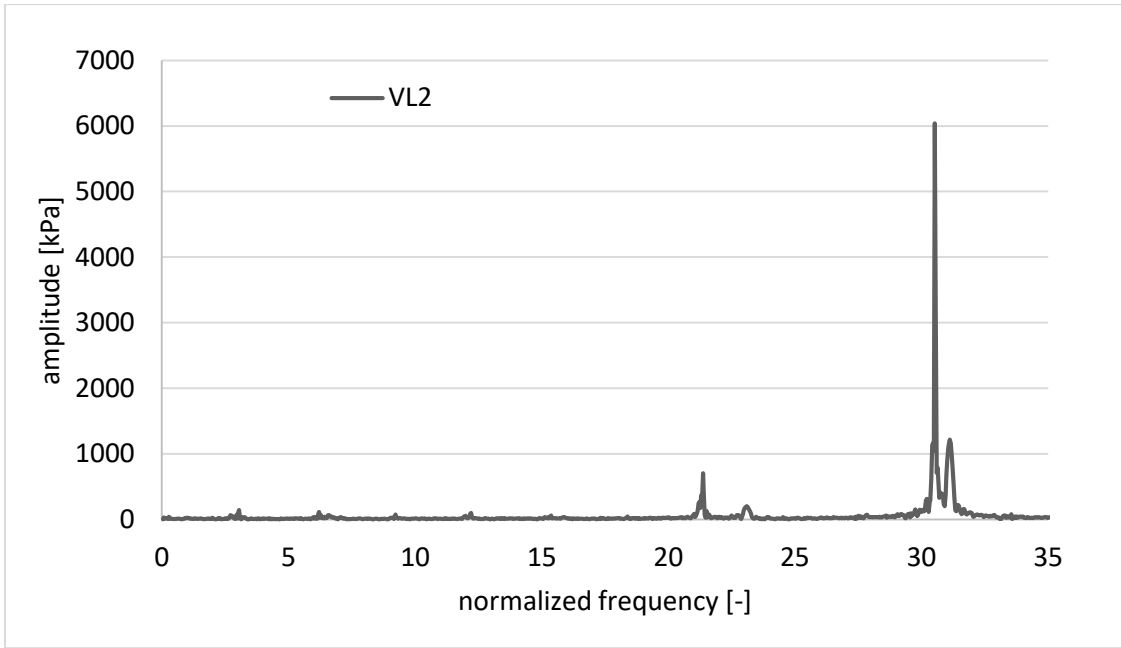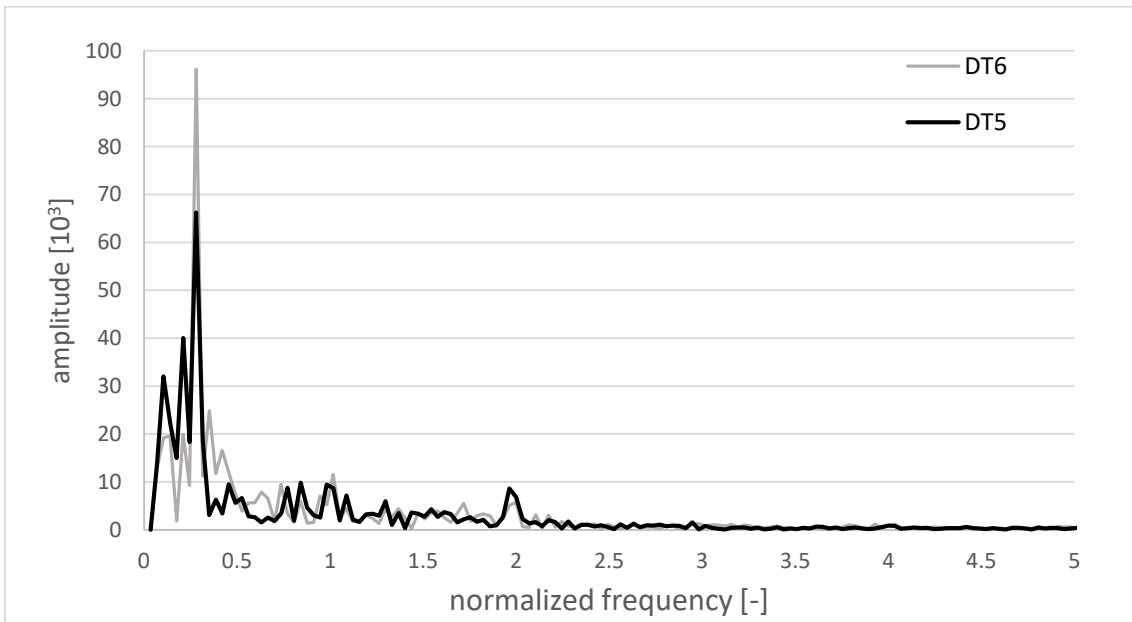
Figure 5.1 FFT analysis of the pressure at VL2

Figure 5.2 FFT analysis for the pressure at DT5 and DT6

Figure 5.3 is shows that the axial velocity in various points on line one has a similar distribution both in the FT3 numerical model and in the experimental results, ranging between a velocity of 2.4m/s in the peripheral area of the draft tube cross section, and 1.5m/s in the core region. It can also be noted that the model predicts well the development of the RVR core region, where the reversed flow encounters.
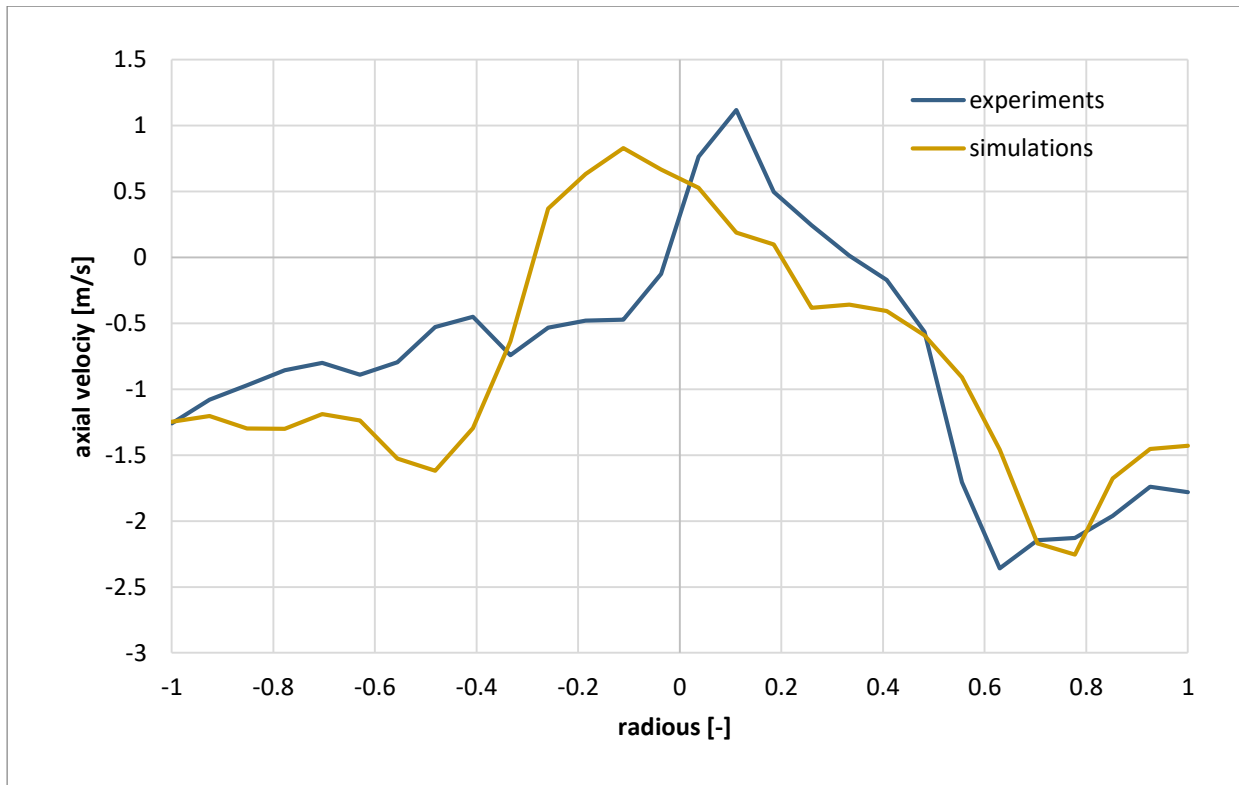
Figure 5.3 Axial velocity distribution along L1 in the draft tube

Based on the above analysis, the numerical model is validated, with a sufficient accuracy for the purpose of this thesis. However, due to the high complexity of the model, the computation time is very long; thus, further improvements of the model must be implemented. A simplified case consisting of just the draft tube domain (DT only), is analyzed and subjected to validation. In the DT only case, the results for head, torque, efficiency and monitor point VL2 cannot be analyzed, as the rotating domain is not modeled; thus, only pressure and the axial velocity distribution are verified for validation. They are completed by a visual check (Figure 5.4) and a sensitivity analysis (Table 5.4) performed to determine whether or not a smaller timestep improves the numerical model convergence. As observed in Figure 5.4, even if the structure of the RVR is not identical in the FT3 and DT only cases, it is predicted fairly well by the reduced model.
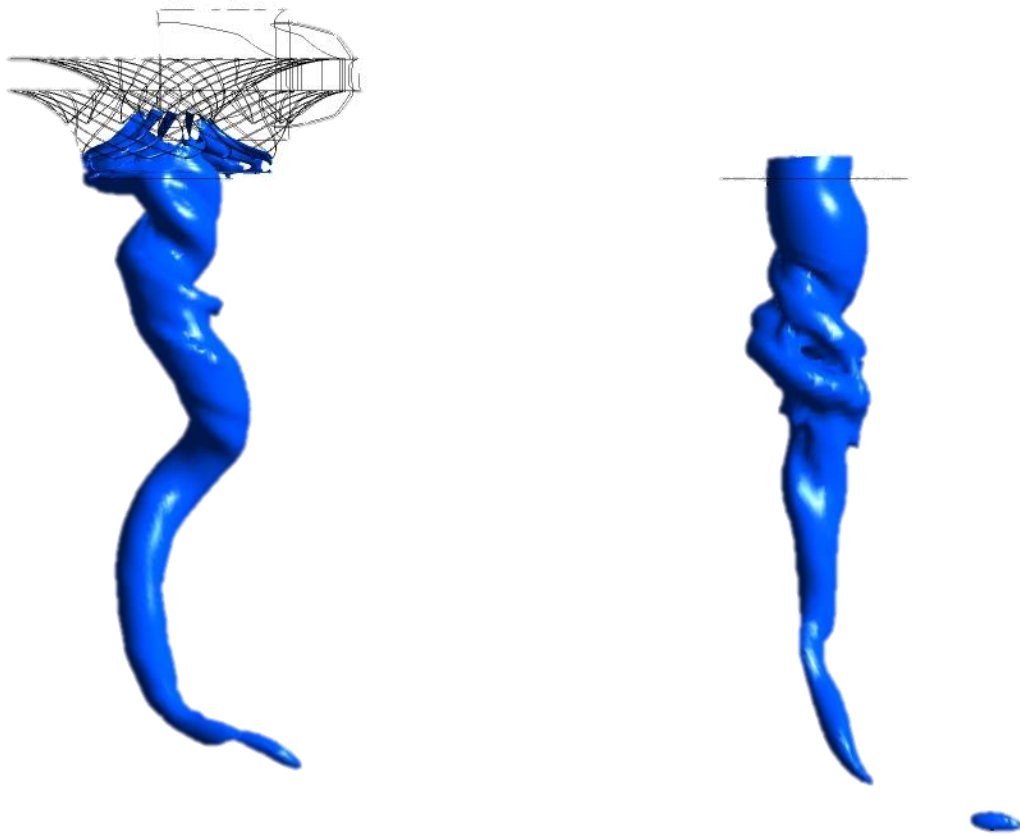
Figure 5.4 Fully developed RVR-visualization through an iso-pressure surface for FT3 (left) and DT only (right)

Table 5.2 FFT analysis for pressure in FT3 and DT only cases

Parameter	Monitor point	Measurements	FT3	DT only	
				5°	2°
Main frequency	DT5	0.32 f_n	0.28 f_n	0.33 f_n	0.36 f_n
	DT6	0.32 f_n	0.28 f_n	0.33 f_n	0.36 f_n
	VL2	30.02 f_n	30.50 f_n	-	-
Amplitude [kPa]	DT5	4263.4	66.2	48.6	136.8
	DT6	1988.1	96.1	40.42	123.5
	VL2	7793.0	6004.4	-	-

A summary of the pressure frequencies and amplitudes from the measurements, FT3 and DT only cases is in Table 5.2. As observed, in both reduced models, the main frequency is the same for the two monitor points in the draft tube (DT5 and DT6), being $0.33f_n$ in DT only 5°, and $0.36f_n$, in DT only 2° case. These frequencies are associated with the presence of RVR in the draft tube. A shift of the RVR frequency is observed in both cases, but the present values lie in the RVR frequency spectrum. In Figure 5.5 an FFT analysis of the pressure frequencies is presented, In all the models, there is good agreement between the maximum amplitude in the two monitor points (DT5 and DT6), but significant discrepancies between the amplitudes in the different simulations.
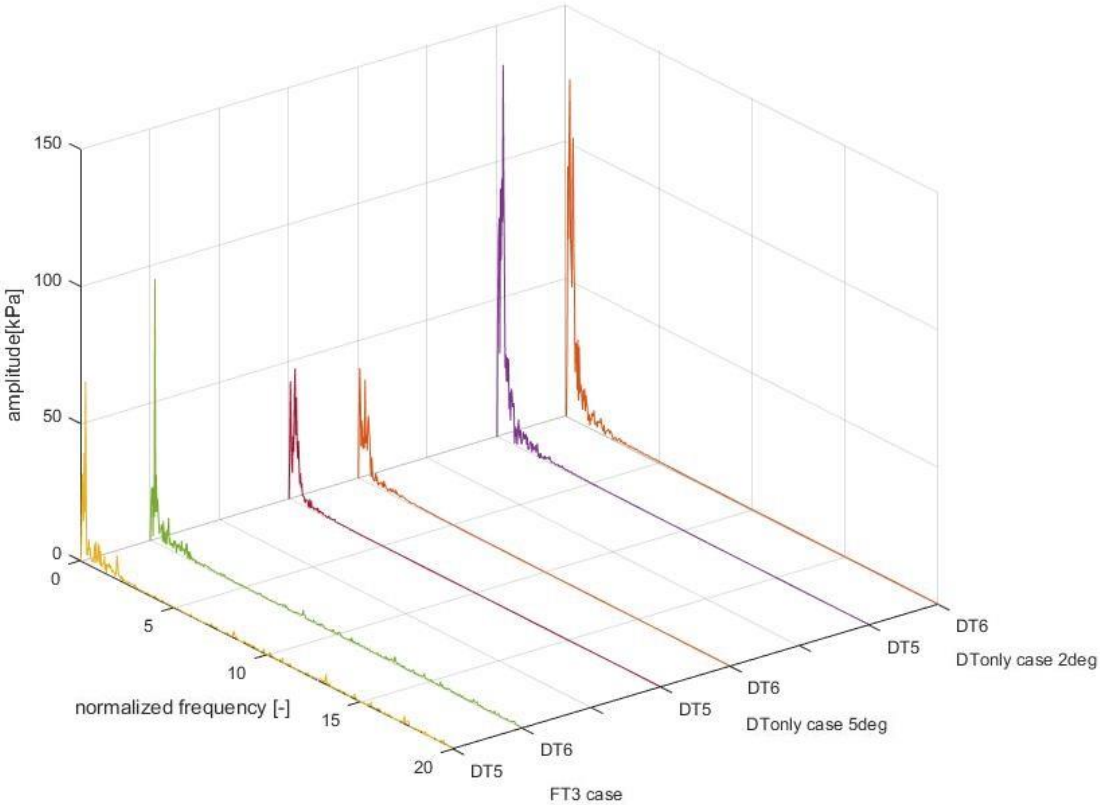

Figure 5.5 Frequency spectrum of pressure in DT only case for monitor point DT5 and monitor point DT6

Figure 5.6 shows that the distribution of the axial velocity along L1 in the draft tube is captured correct in the DT only cases, which validates the reduced model as capable of modelling the flow pattern and capturing the characteristics of vortex breakdown phenomenon.
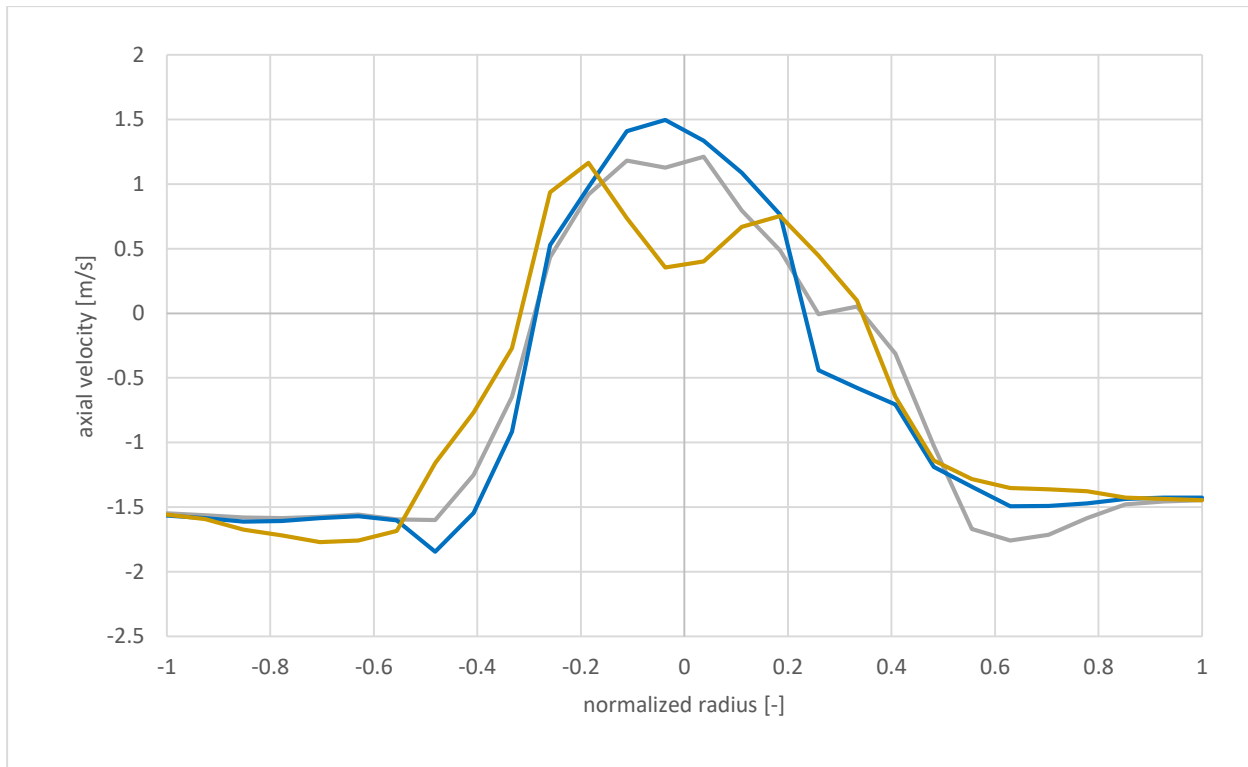
33

Figure 5.6 Axial velocity distribution in various points on L1 at different timesteps

In the simplified model, the flow rate at the DT inlet decreases from 0.1373 m^3/s to 0.1337 m^3/s, as shown in Table 5.3. This is attributed to the new boundary conditions, as these are determined from interpolated data and not from measurements, thus small discrepancies are acceptable. It can also be observed that the main frequency determined both from pressure and velocity data are the same in each case, even if they differ from one case to another.

Table 5.3 Flow parameters for full runner and simplified cases

Analyzed parameter	FT3 (5°)	DT only (5°)	DT only (2°)
Number of runner rotations before RVR starts to form [-]	2	2.5	2.5
Flow rate at inlet [m3/s]	0.1373	0.1337	0.1337
RVR frequency from pressure [-]	0.28 f_n	0.33 f_n	0.36 f_n
RVR frequency from axial velocity [-]	0.28 f_n	0.33 f_n	0.36 f_n
Pressure at DT inlet [kPa]	116.06	116.07	116.05

As both cases yield realistic results, capturing the main phenomenon, a computational effort analysis is performed based on the total required simulation time T, as shown in equation (5.1), where t is the elapsed time until flow stability is reached.

Table 5.4 shows that, as expected, the smallest computational effort is obtained in DT only 5° case, thus the following simulations are developed based on the numerical model of this case.

$$T = t + 5[s] \qquad\qquad (5.1)$$

Table 5.4 Computational time usage improvement

Analyzed parameter	Parameter notation	full runner (5°)	DT only (5°)	DT only (2°)
Time until stable flow reached [s]	t	1.2	1.9	1.5
Total required simulation time [s]	T	6.2	6.9	6.5
Computational effort [CPU hours]	-	6050	268.5	418.6

5.2 Constant air injection

In this section, the results for air injection at different flow rates through a 30mm diameter nozzle are presented. Only the most conclusive results are discussed, with the aim of determining the optimal quantity of injected air for mitigating the effect of RVR.

Figure 5.7 representes the pressure response at the draft tube wall (point DT5) for a constant air flow rate of 1% of the water flow rate. The dashed line at 10s indicates the start of AI, which is implemented as a step function. The influence of air injection is recorded at the draft tube wall after 1.7s, and after 2.3s more, the system reaches a steady state. In addition, a decrease in the pressure fluctuations of 35%, from 0.34kPa to 0.12kPa is observed. For the pressure signal presented in Figure 5.7, an FFT analysis is done in Figure 5.8. The red line represents the analyzed signal during operation with no air injection, the green line represents the analyzed signal during 1% constant air injection, after system stabilization, and the black lines are system stabilization times. As observed, the RVR amplitude is halved due to air injection.
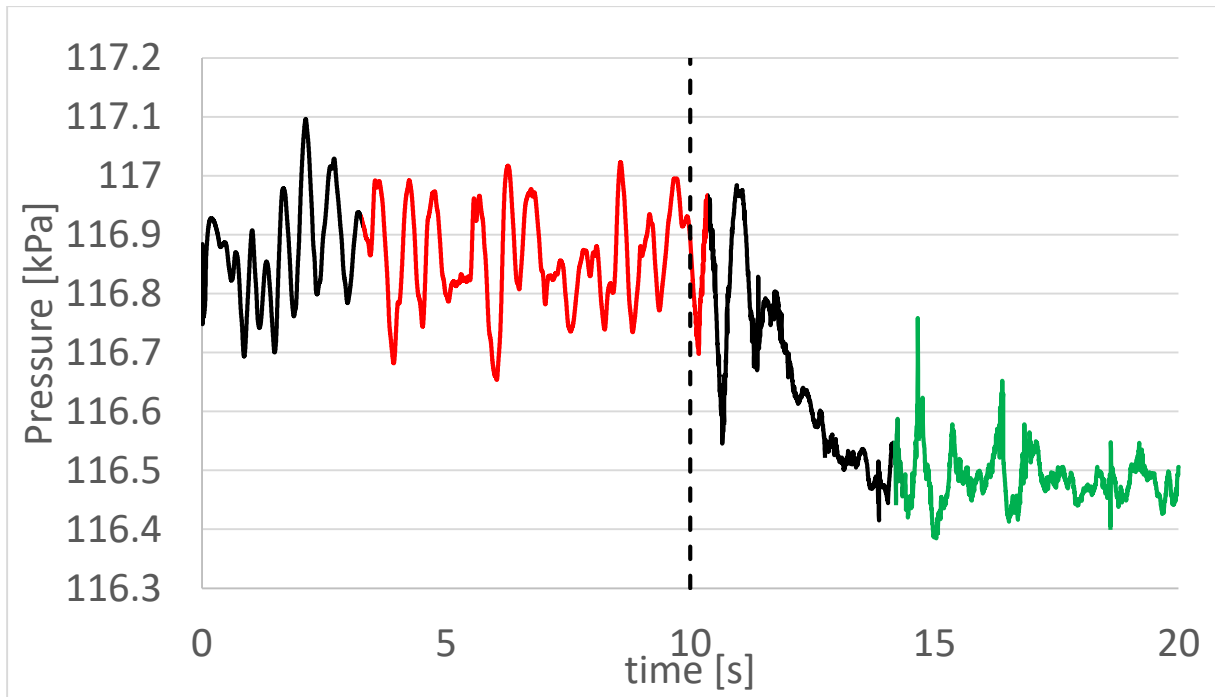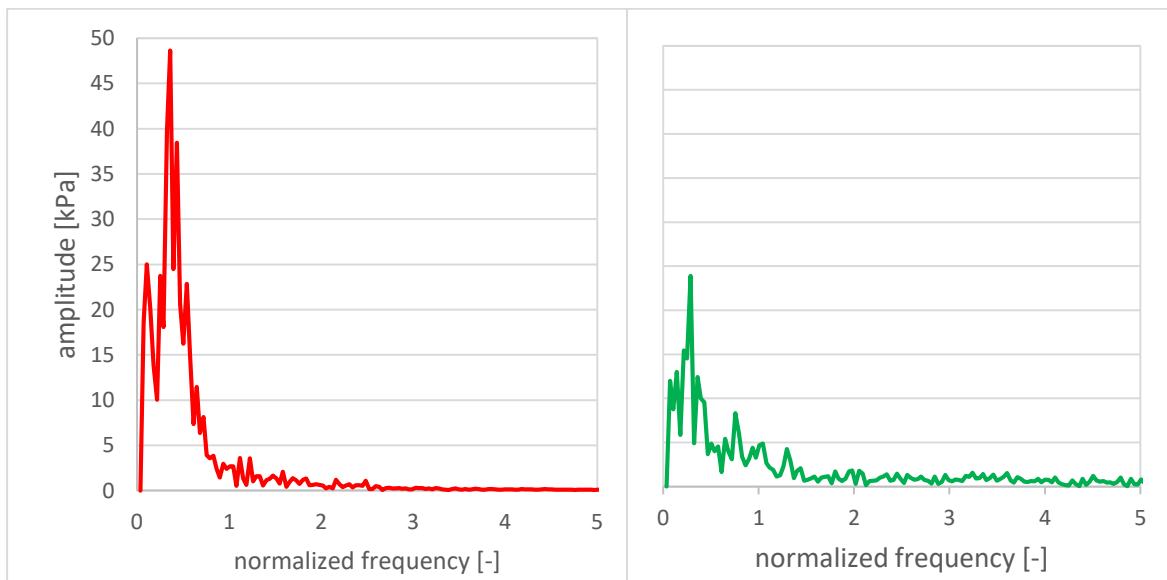
Figure 5.7 Pressure response at DT5 for 1% AI

Figure 5.8 FFT for pressure response at DT5 for AI 0% (left) and 1% (right)

In Appendix A and Appendix B, the pressure responses for the four studied cases are presented for the pressure monitor points DT5 and DT6, respectively. The results summarized in Table 5.5 show that, with the increase of Qair, the system response time decreases. As for the change in the pressure fluctuation, the highest decrease is obtained for Qair/Qwater of 1%. It is also important to note that, after a certain AI value, the air tends to destabilize the system, instead

36

of stabilizing it, as shown in the 3% case, where the pressure fluctuations increase due to the AI, in comparison to the other cases where they decrease to a certain extent. As an extra verification of the last statement, an extra simulation with Q_{air}/Q_{water} of 10% is run (Appendix C), showing an increase of 85% in the pressure fluctuations.

Table 5.5 Pressure signal analysis for monitor point DT5 and 30mm nozzle

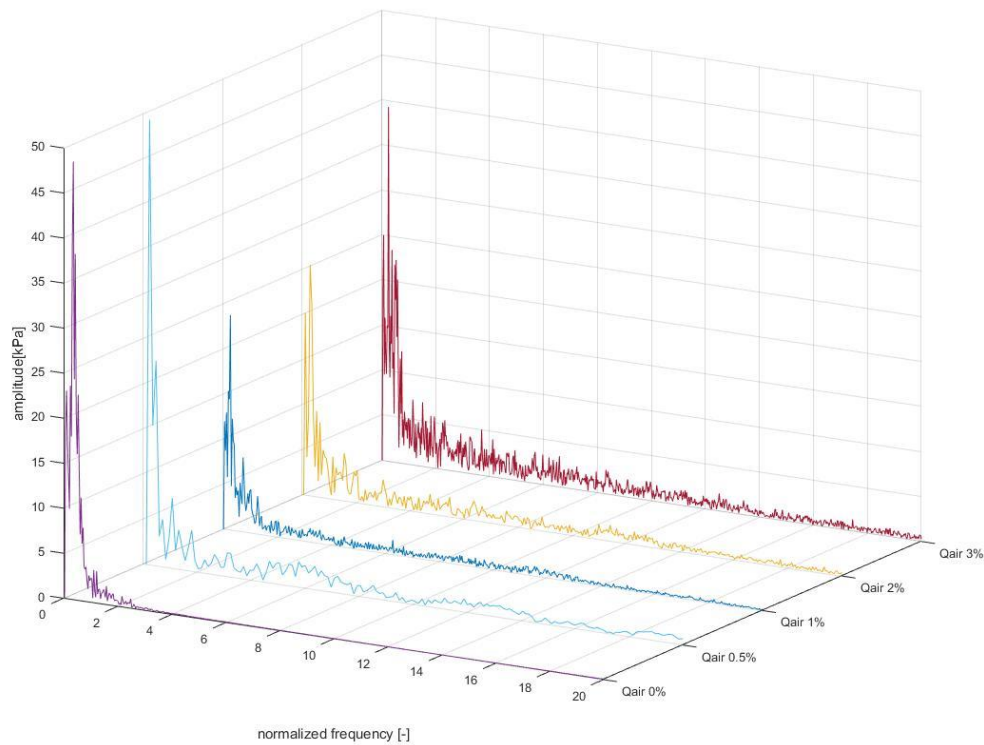| Q_{air}/Q_{water} ⟍ Parameter	0.5%	1%	2%	3%
System response time[1] [s]	2.3	1.7	1.3	1
System stability time[2] [s]	8.3	4	6	2.6
Pressure fluctuation change [%]	-54%	-60%	-25%	+10%

Figure 5.9 FFT analysis of the pressure in point DT5 during constant air injection

An FFT analysis of the pressure at DT5 for all 4 air flow rates is shown in

Figure 5.9, with the results summarized in Table 5.6. The main observed frequency in all cases lies between $0.24f_n$ and $0.30f_n$, which corresponds to a shifted RVR frequency, from the $0.33f_n$

---

[1] Time elapsed between the start of AI and the moment it starts to influence the pressure on the draft tube wall
[2] Time elapsed between the start of AI and the moment when the system stability is reached

frequency, when there is no air injected. The amplitude of the RVR decreases from 48.6 kPa in the 0% air case, to less than 40 kPa in most AI cases (1%, 2% and 3%).

Table 5.6 FFT results for the constant air injections studied cases

Q_{air}/Q_{water} Parameter	0 %	0.5%	1%	2%	3%
Normalized main frequency [-]	0.33 f_n	0.24 f_n	0.29 f_n	0.30 f_n	0.25 f_n
Amplitude [kPa]	48.6	49.4	23.4	25.6	39.6

Figure 5.10 presents the variation of RVR amplitude function of the air injection rate, where the dashed line represents the RVR amplitude when no air is injected in the system. In 0.5% AI case there is a slight increase of the RVR amplitude, which is likewise observed by Yu [24]. The amplitude of the RVR decreases the most in the 1% case, where it becomes 48% of the no air injection case. Considering the presented results, the 1% AI case is selected as the best-case scenario. The velocity profile is further checked for this case, in order to verify the consistency of the results.
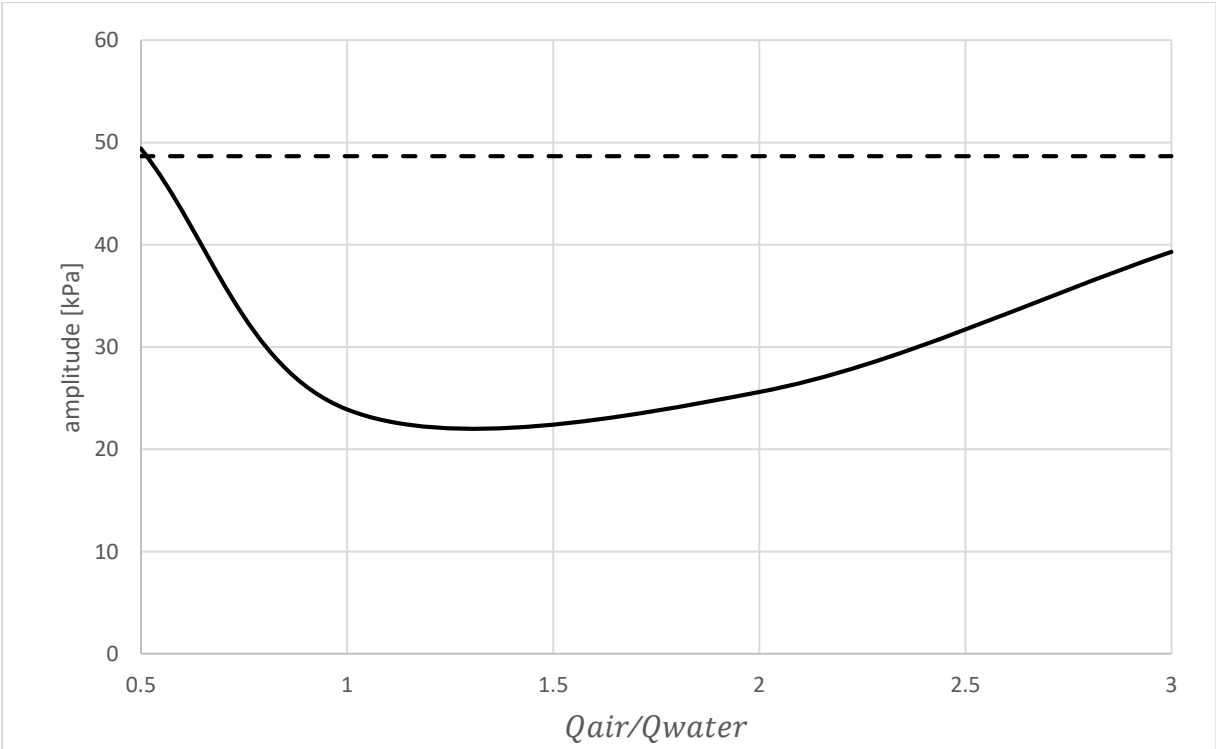

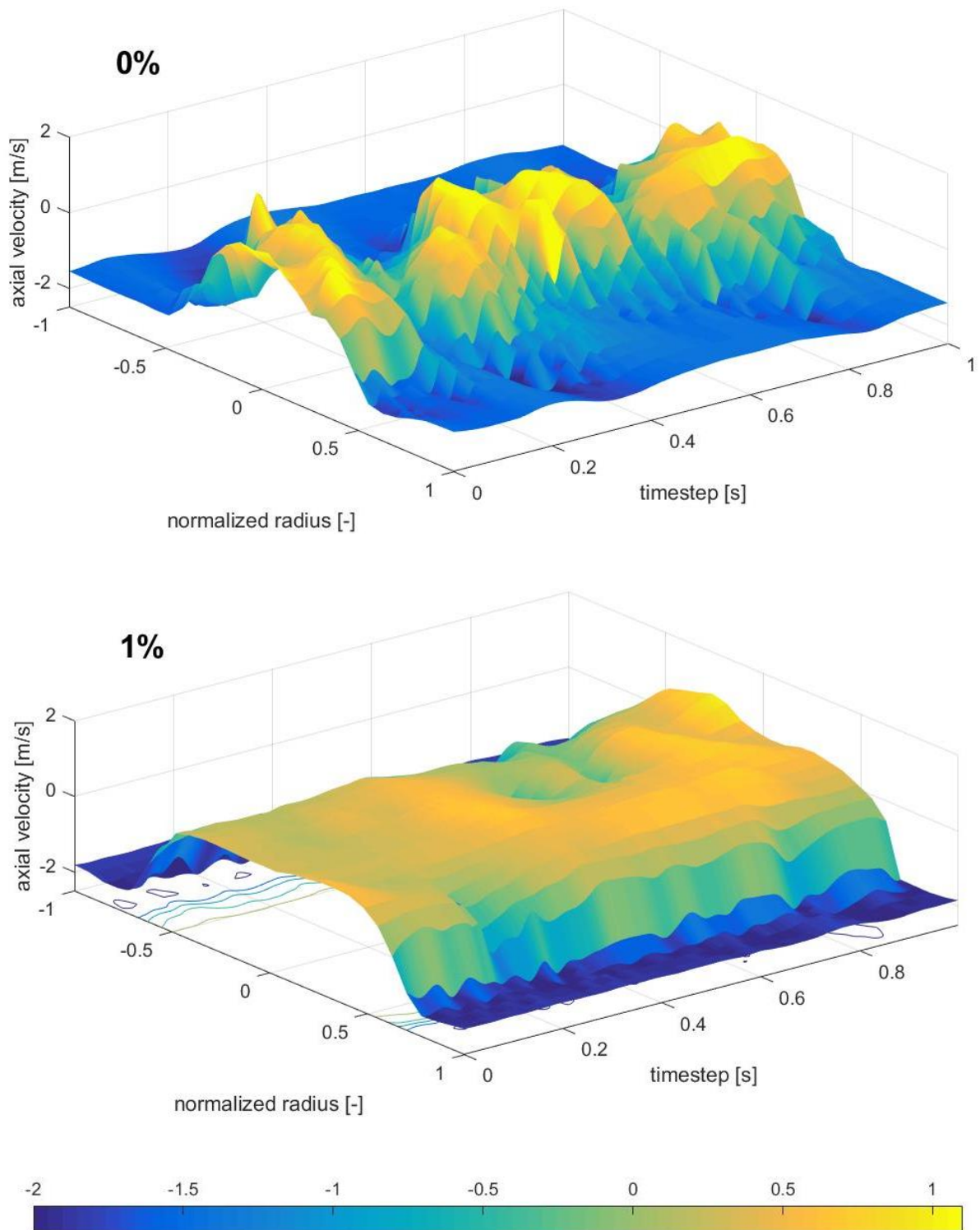**Figure 5.10 RVR amplitude function of the air injection rate**

Figure 5.11 Axial velocity variation in time along L1

Figure 5.11 presents a spatial and temporal variation of the axial velocity for 0% and 1% air injection along L1 for a total time of one second. When air is injected, significant improvements can be observed in terms to velocity fluctuations, both close to the wall and in the center of the draft tube. The axial velocity is more stable, and also presents a decrease of the maximum axial

velocity in the core zone from 1.2 m/s to 0.9 m/s. A more stable velocity profile is achieved close to the DT wall as well, with fluctuations decreasing to less than half of the ones before air injection. The same can be observed in Figure 5.12. Graphs similar to the ones in Figure 5.11 are presented in Appendix D.

The dashed line in Figure 5.12 marks the beginning of the air injection. Similar to the pressure response on the draft tube wall from Figure 5.7, the system response is not immediate, but after 1.2 seconds. The system stability time is the same as for the pressure response, four seconds being necessary reach a steady state.
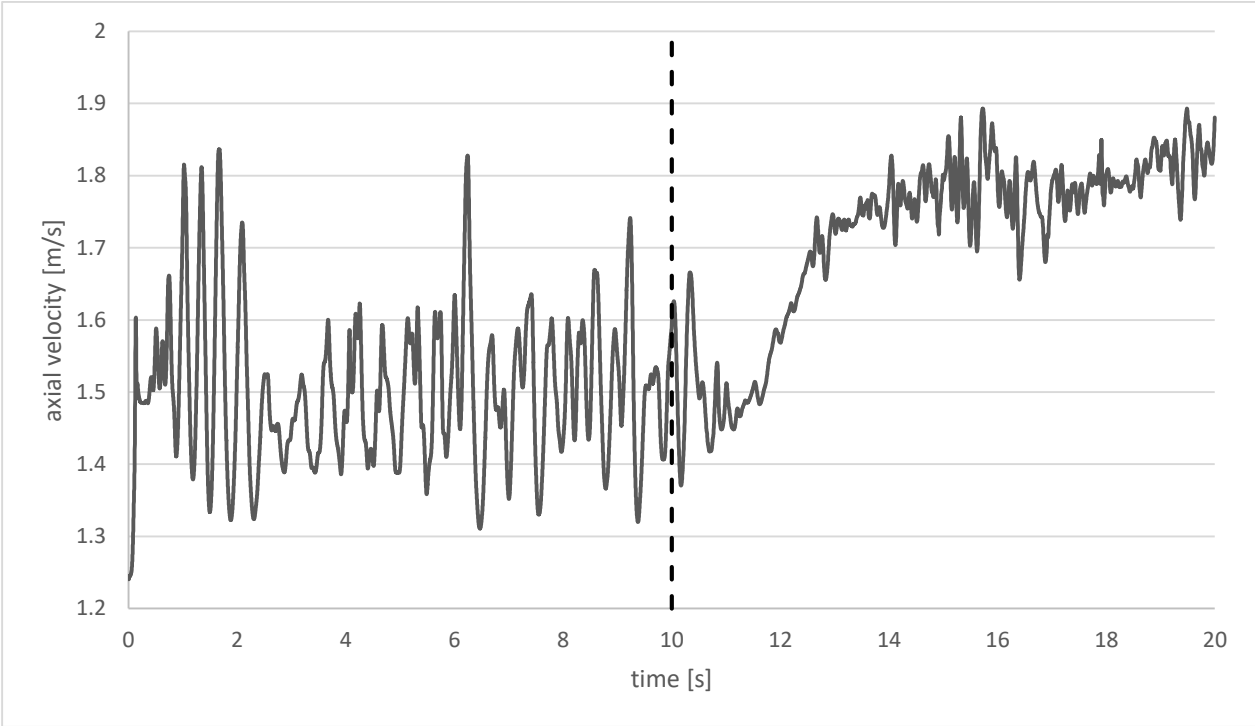

Figure 5.12 Axial velocity variation near the draft tube wall, on L1

From the analyzed cases, the 1% constant AI is optimal for mitigating the effect of the RVR. Thus, this specific case is further analyzed for improving its effects by varying the injected air flow rate.

5.3 Variable air injection

In this section, the possibility of varying the air flow rate is analyzed, in order to either decrease the necessary quantity of air or improve the system response to the air injection by decreasing the effects of RVR. The presented cases are modeled based on the optimum results obtained in the constant air injection case (i.e. 1% constant air injection). In order to have a smooth variation

in flow rate, a sinusoidal transition is implemented in all cases. The results are presented in order, as a step-by-step model development.

Before implementing any variation case, an analysis of system response to nozzle closure is done as shown in Figure 5.13, in order to determine the pressure response to a decrease of the air flow rate. The single dashed line marks the moment when the air injection starts and the double dashed line represents the moment of nozzle closure.
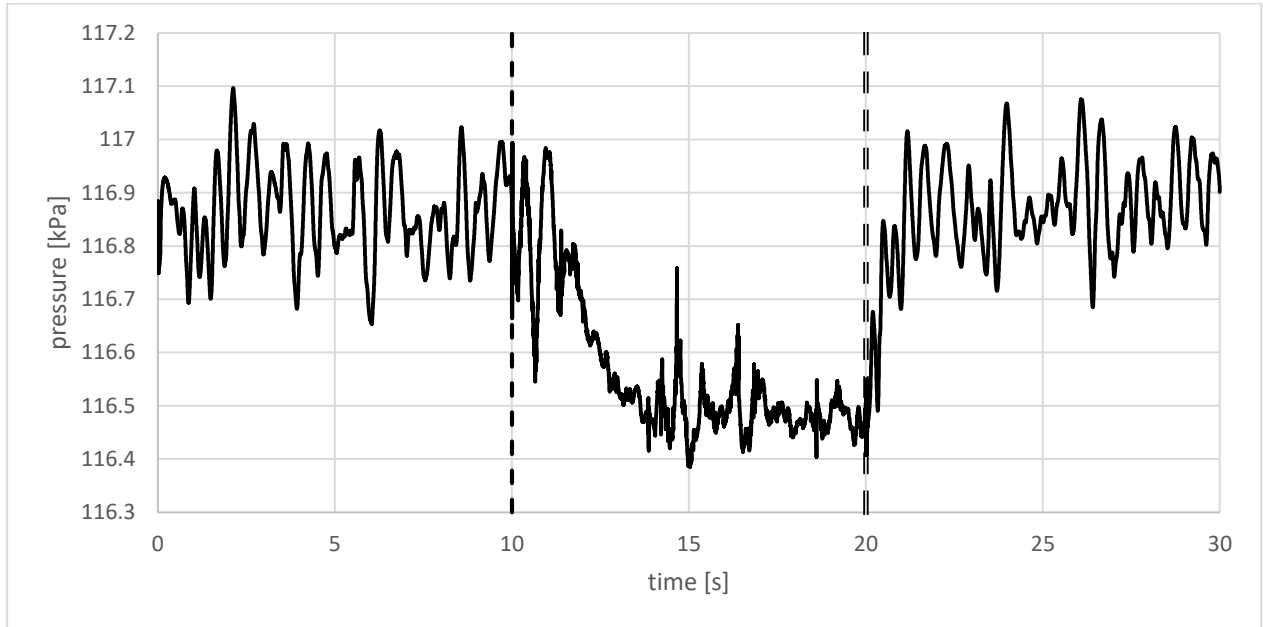

Figure 5.13 Pressure response for nozzle closure

As observed in Figure 5.13, the system response time at the start of AI is 1.7 seconds, reaching system stability after four seconds. In the AI stop case (nozzle closed), the system response time is very short, reasonably approximated as an instant response. In the nozzle closure case, the system stability time is one second, meaning that it responds four times faster to air shut-down than to air turn-on. As a result, the frequency of the pulsating air injection has to be higher than 1 Hz, so that RVR does not have time to develop. However, this case does not show what the optimal frequency would be. As the aim of the study is to mitigate the pressure fluctuation induced by the presence of RVR, a variable air injection with the same frequency as RVR is expected to give accurate results. For validation of this assumption, two cases are compared: the first one has a variable AI with the RVR frequency, and the second with 3.5 times higher frequency than f_{RVR}. The value of the frequency in the second case is randomly picked, following just one rule: it should differ from the runner frequency in order to avoid non-

41

independent frequency results. The outcome of this comparison is shown in Figure 5.14. The mitigation of RVR is similar in the two cases, but when air is injected with a higher frequency than f_{RVR}, the AI frequency appears in the system with a larger amplitude than f_{RVR}. Thus, the previous assumption proves right and is used in the analysis of the next step.
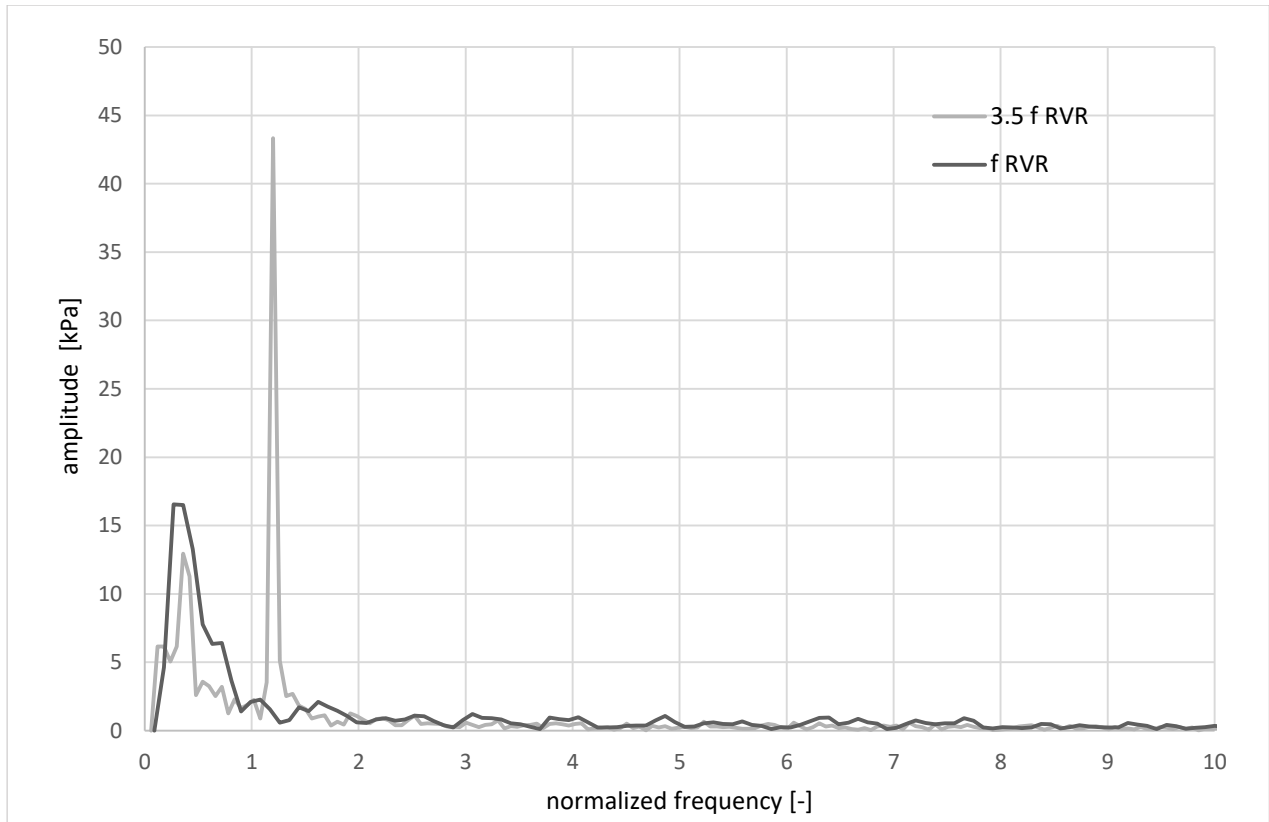

Figure 5.14 FFT analysis for different AI pulsating frequencies

Another important aspect of the air injection variation is the phase. As shown by [13], the plunging component of RVR starts to develop before the rotating component. Thus, for a start of AI in counter phase with the plunging component phase, an improvement of the mitigation method is expected. This is checked by two simulations: air injection started in phase and in counter phase with the plunging component. As shown in Figure 5.15, the amplitude of the AI in counter phase with the plunging component is lower than that of the in phase case. Even if the amplitude of both cases exceeds the RVR amplitude with no mitigation [see Part load in

42

Results and discussions chapter], the focus of this case is to determine the correct phase for AI, so the results is considered successful.
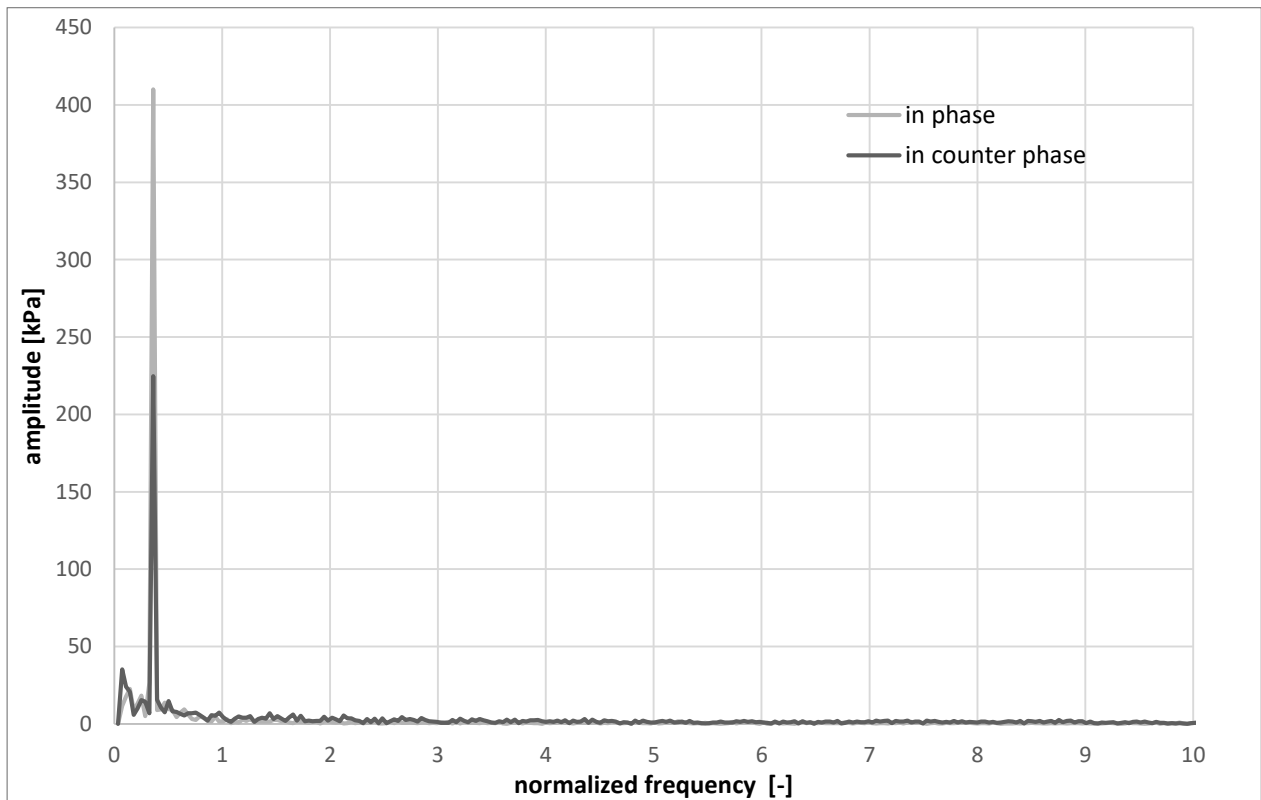

Figure 5.15 FFT analysis of the AI in phase and in counter phase with the plunging component of the RVR

As a small summary of the results obtained for the model build-up, it can be said that the variation of the air injection has to be in counter phase, with the same frequency as the RVR. In addition, the AI variation is implemented as a sinusoid. With this conditions set, the study of ways to improve the AI as an RVR mitigation method is presented below.

For determining the possibility of reducing Q_{air}, three cases are studies, as follows:

- Q_{air} variation between 0 and 1% Q_{water}
- Q_{air} variation between 0.5 and 1% Q_{water}
- Q_{air} variation between 0.9 and 1% Q_{water}

In all cases, the variable air injection starts directly after the nozzle opens, and no preliminary system stabilization is done using constant air injection. Figure 5.16 presents the FFT analysis

of the variable injection cases in comparison with the optimal constant air injection and the no air injection case. It can be noticed that injecting the air with a small variation yields similar results as in the constant air injection case, both being less than half of the RVR amplitude in the no air injection case. With the increase of variation, the RVR amplitude increases, meaning that higher pressure-fluctuations are present in the draft tube. This is contrary to the aim of injecting air, thus only a small variation of the AI is feasible for implementation. When it comes to the RVR frequency, it remain the same in all cases, with no notable frequency shift.
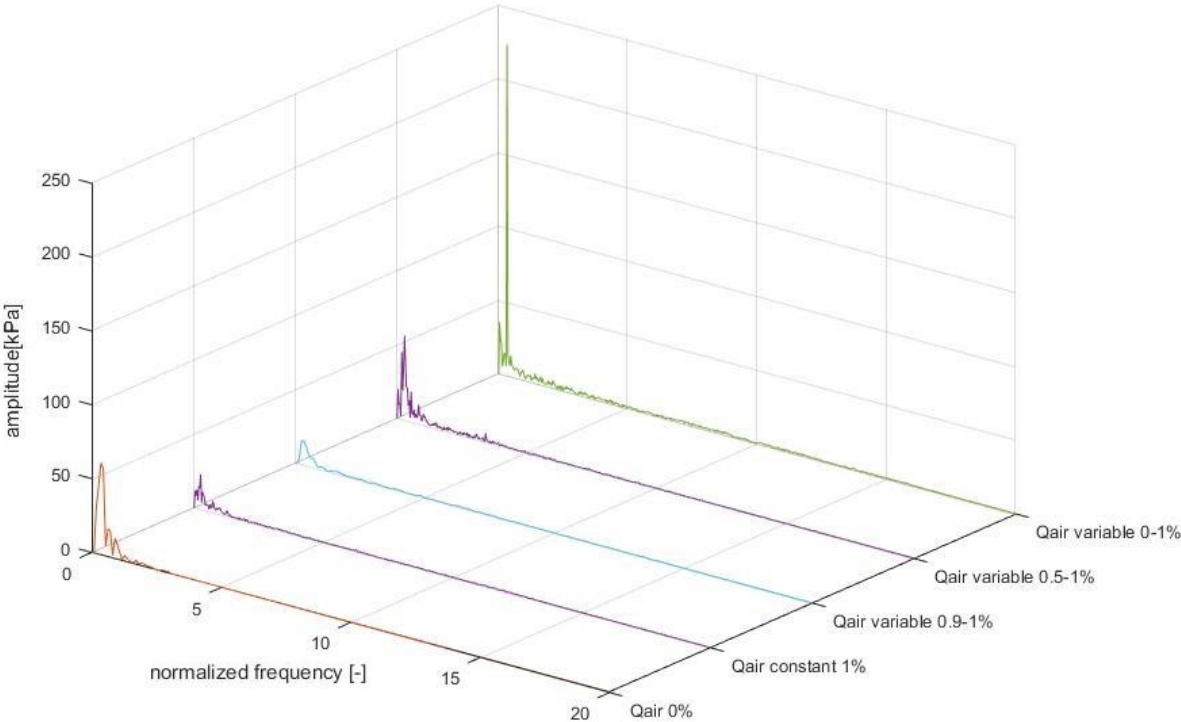

Figure 5.16 FFT analysis of variable air injection with no preliminary system stabilization

6 Conclusion

The purpose of this project was to investigate potential improvements to air injection methods, towards reducing the amount of air necessary for mitigating the pressure fluctuations of the RVR while maintaining the system efficiency.

One numerical model was developed for simulating the part load operation of a Francis model, and the obtained results were analyzed and compared to experimental data for validation. The model was further updated to a multiphase flow model, in order to simulate air injection in the draft tube of a turbine and its effects, along with possible improvements. Parametric and comparative studies were carried on for all relevant cases. Following are the main findings:

1. In the part load simulation DT only case, the RVR is developing fairly accurately, showing that the reduced domain is able of capturing the vortex breakdown phenomenon and the correct flow pattern.

2. As the computational effort is an important aspect, a 5° timestep is sufficient for simulating the part load condition in the draft tube of a Francis turbine, yielding similar results as the 2° timestep and the measurements. In addition, for accuracy of results, a simulation time of 10 seconds is ideal, in order to reach a stable regime and collect enough data for flow analysis.

3. A small amount of air injected in the draft tube of a turbine changes the flow characteristics, leading to a significant decrease of the pressure pulsation amplitude encountered due to the rotating vortex rope. On the other hand, air injection is actually detrimental in case of injecting too large a quantity of air.

4. The influence of the air is observed at the monitor points on the draft tube after 9.4 runner rotations, while after closing the air injection system the RVR develops four times faster. This proves that the frequency for varying air injection has to be smaller than then two runner rotations.

5. The air should be injected with the same frequency as the RVR, because injecting air with other frequencies tends to introduce extra pressure fluctuations in the system.

6. While small variations of air injection improve or maintain the flow characteristics as in the constant air injection case, a large variation destabilizes the system.

Generally, the conclusion is that variable air injection is a feasible method which needs more investigation for improvement.

7 Further work

As the scope of this thesis was to set the basis for new possibilities regarding the air injection methods, the developed model is simplistic. Thus, many further work possibilities are open in order to improve the model accuracy. Among the most important is getting measurement data for a better model validation. On the modelling side, necessary improvements in regard to implementing a compressibility model or analyzing the system response to decreased timestep should be implemented.

A key interest that can be researched is implementing a 3-phase flow (water-vapor-air), in order to model the air response to vapor cavities formation during very low pressure in the draft tube. In addition, simulating the full runner case could be of interest as well, so that a good overview of the effect of varying air injection is obtained.

Finally, a technical-economical study should be realized, as implementing a pulsated air injection system is probably more expensive than the system for providing a constant air supply. Doing a cost-benefit analysis is crucial for getting an overview of the development possibilities for the method.
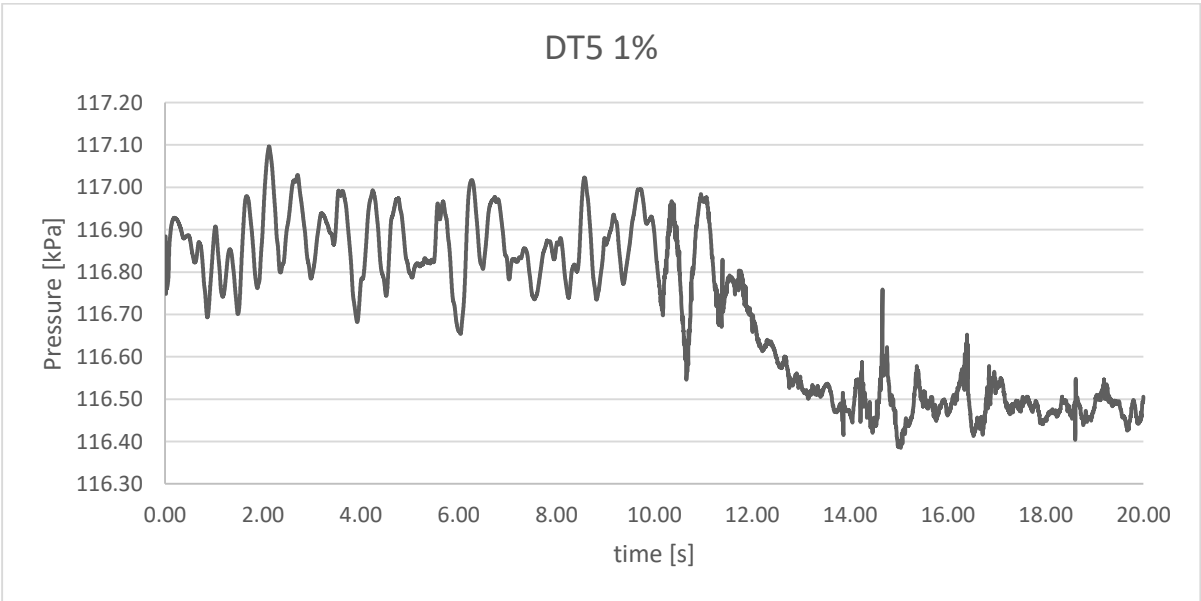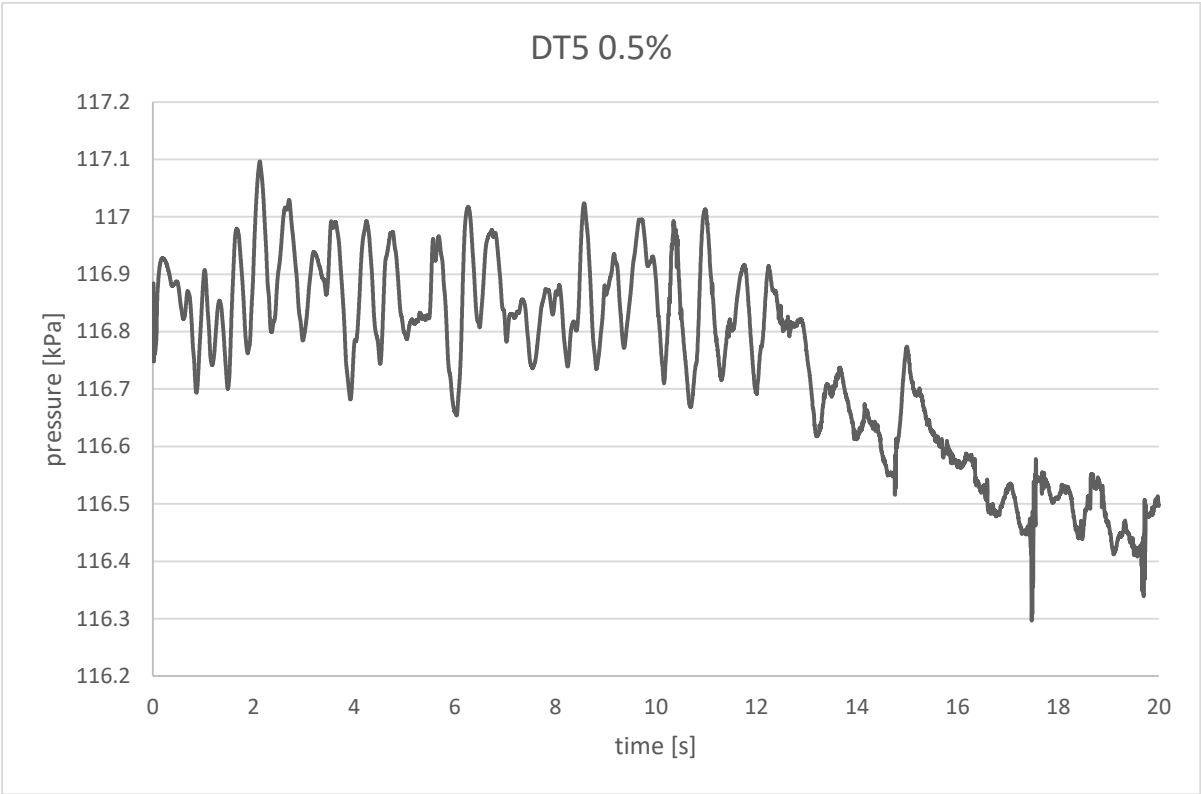
8 References

[1] "Skeptical Science," Skeptical Science, [Online]. Available: https://www.skepticalscience.com/print.php?r=374.

[2] A. Baya, S. Muntean, V. Campian, M. Diaconescu and G. Balan, "Experimental investigations of the unsteady flow in a Francis turbine draft tube cone," in *IOP Conf. Series: Earth and Environmental Science*, Nanjing, 2010.

[3] F. Casanova, "Failure analysis of the draft tube connecting bolts of a Francis-type hydroelectric power plant," *Engineering Failure Analysis,* vol. 16, pp. 2202-2208, 2009.

[4] V. Turkmenoglu, "The vortex effect of Francis turbine in electric power generation," *Turkish Journal of Electrical Engineering & Computer Sciences,* vol. 21, pp. 26-37, 2013.

[5] P. Dorfler, "Design Criteria for Air Admission Systems in Francis Turbines," in *IAHR Symposium*, Montreal, 1986.

[6] R. Susan-Resiga, T. Vu, S. Munteanu, G. D. Ciocan and B. Nennemann, "Jet Control of the Draft Tube Vortex Rope in Francis Turbines at Partial Discharge," in *23rd IAHR Symposium Proceeding*, Yokohama, 2006.

[7] P. Dorfler, M. Sick and A. Coutu, Flow-Induced Pulsations and Vibrations in Hydroelectric Machinery, Springer, 2013.

[8] J. Cassidy and H. Falvey, "Frequency and amplitude of pressure surges generated by swirling flow," in *IAHR Section Hydraulic Machinery, Equipment, and Cavitation, 5th Symposium*, Stockholm, 1970.

[9] M. Melot, B. Nennemann and N. Desy, "Draft tube pressure pulsation in Francis turbines with transient Computational Fluid Dynamics methodology," in *IOP Conf. Series: Earth and Environmental Science 22 (2014)*, 2014.

[10] M. Nichi, T. Kubota and S. Matsunaga, "Surging characteristics of conical and elbow-type draft tubes," in *IAHR Section Hydraulic Machinery, Equipment, and Cavitation, 12th Symposium*, Stirling, 1984.
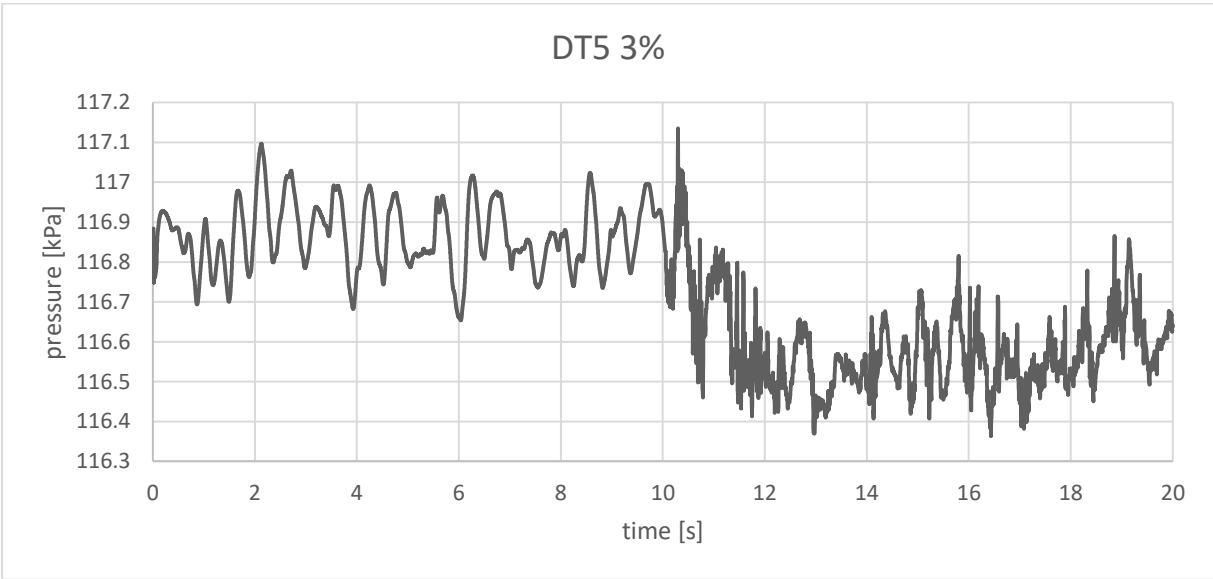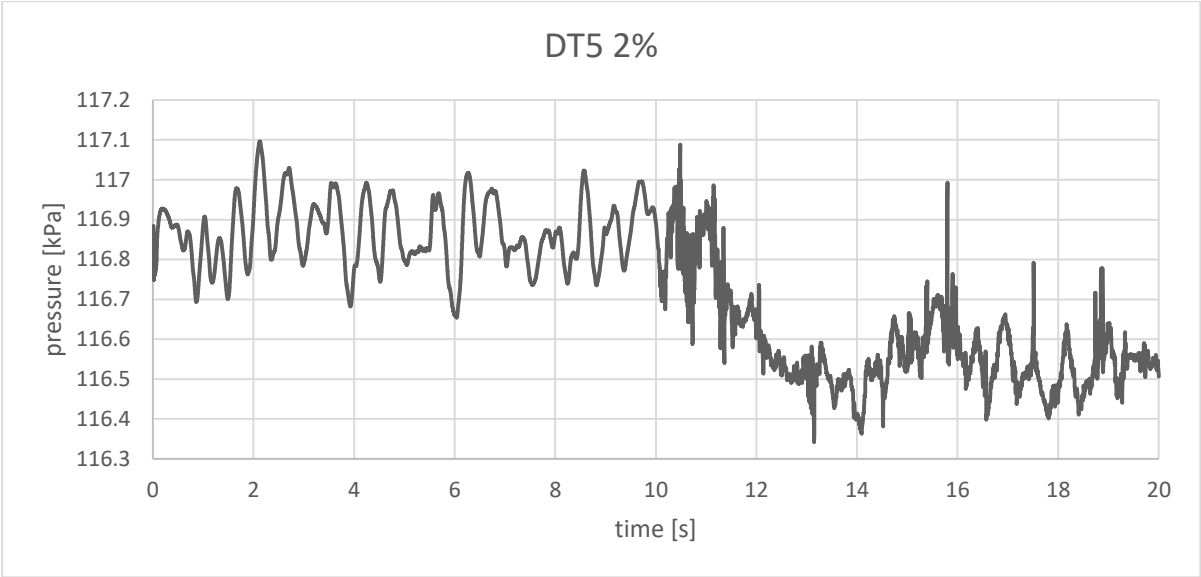
[11] K. Koutnik, K. Kruger, F. Pochyly, P. Rudolf and V. Haban, "On Cavitating Vortex Rope Form Stability During Francis Turbine Part Load Operation," in *International Meeting of the Workgroup on Cavitation and Dynamic Problems in Hydraulic Machinery and Systems*, Barcelona, 2006.

[12] K. Amiri, M. Cervantes and B. Mulu, "Experimental investigation of the hydraulic loads on the runner o a Kaplan turbine model and the corresponding prototype," *Jurnal of Hydraulic Research,* vol. 4, no. 53, pp. 452-465, 2015.

[13] R. Goyal, M. J. Cervantes and B. Gandhi, "Vortex rope formation in a high head model Francis turbine," *Journal of Fluid Engineering,* 2016.

[14] A. Bosioc, R. Susan-Resiga, S. Munteanu and C. Tanase, "Unsteady pressure analysis o a swirling flow with vortex rope and axial water injection in a discharge cone," *Jurnal of Fluids Engineering,* 2012.

[15] P. Hopping, P. March and P. Wolff, *Justifying, Specifying, and Verifying Performance of Aerating Turbines.*

[16] P. March, "Hydraulic and Environmental Performance of Aerating Turbine Technologies," in *Proceedings of EPRI/DOE Conference on Environmentally-Enhanced Hydropower Turbines*, Palo Alto, Calofornia, 2011.

[17] M. Angulo, A. Rivetti, L. Diaz and S. Liscia, "Air injection test on a Kaplan turbine: prototype – model comparison," in *IOP Conf. Series: Earth and Environmental Science*, 1016.

[18] R. Arndt, S. Paul and C. Ellis, "Investitation of the Use of Air Injection to Mitigate Cavitation Erosion," St. Anthony Falls Hydraulic Laboratory, University of Minnesota, Minneapolis, 1993.

[19] S. Adolfsson, *Expanding operating ranges using active flow control in Francis turbines,* Umeå: Bachelo thesis - Department of Applied Physics and Electronics, Umeå University, 2014.

[20] R. Huang, A. Yu, X. Luo and B. Ji, "Numerical Simulation of Pressure Vibrations in a Francis Turbine Draft Tube with Air Admission," in *Proceedings of the ASME 2014 4th Joint US-European Fluids Engineering Division Summer*, Chicago, 2014.

[21] K. Rohland, J. Foust, G. Lewis and J. Sigmon, "HydroWorld - Equipment: Aerating Turbines for Duke Energy's New Bridgewater Powerhouse," 2010. [Online]. Available: www.hydroworld.com. [Accessed 2016].

[22] C. Nicolet, *Hydroacoustic Modelling and Numerical Simulation of Unsteady Operation of Hydroelectric Systems - PhD Thesis,* Lausanne: EPFL n°3751, 2007.

[23] H. Foroutan, *Simulation, Analysis and Mitigation of Vortex Rope Formation in the Draft Tube of Hydraulic Turbines,* Philadelphia: The Pennsylvania State University, College of Engineering, 2015.

[24] A. Yu, X. Luo and B. Ji, "Numerical simulation and analysis of the internal flow in a Francis turbine with air admission," in *IOP Conference Series: Materials Science and Engineering 72*, 2015.

[25] F. Bunea, G. Ciocan, G. Oprina, G. Baran and C. Babutanu, "Hydropower impact on water quality," *Environmental Engineering and Management Journal,* vol. 59, no. 11, pp. 1459-1464, 2010.

[26] *ANSYS CFX Theory Guide.*

[27] F. Menter and Y. Egorov, "The Scale Adaptive Simulation Method fo Unsteady Turbulent Flow Predictions. Part 1: Theory and Model Description.," *Flow, Turbulence and Combustion,* no. 85, pp. 113-138, 2010.

[28] P. Ostly, J. T. Bildal, B. Haugen and O. G. Dahlhaug, "On the relation between friction losses and pressure pulsations caused bt Rotor Stator interaction of Francis-99 turbine," in *Francis 99, Second Workshop*, Trondheim, 2016.

[29] Y. Dewan, C. Custer and A. Ivashchenko, "Simulation of the Francis-99 Hydro Turbine During Steady and Transient Operation," in *Francis 99, Second workshop*, Trondheim, 2016.

[30] E. Casartelli, L. Mangani, O. Ryan and A. Del Rio, "Performance prediction of the high head Francis-99 turbine for steady operation points," in *Francis 99, Second workshop*, Trondheim, 2016.
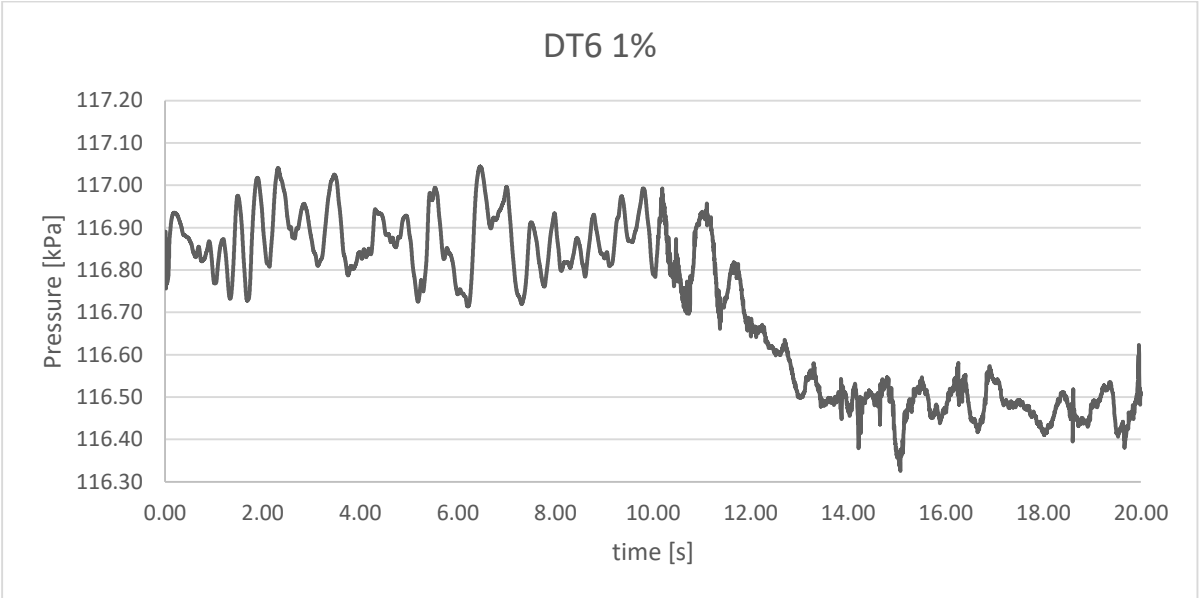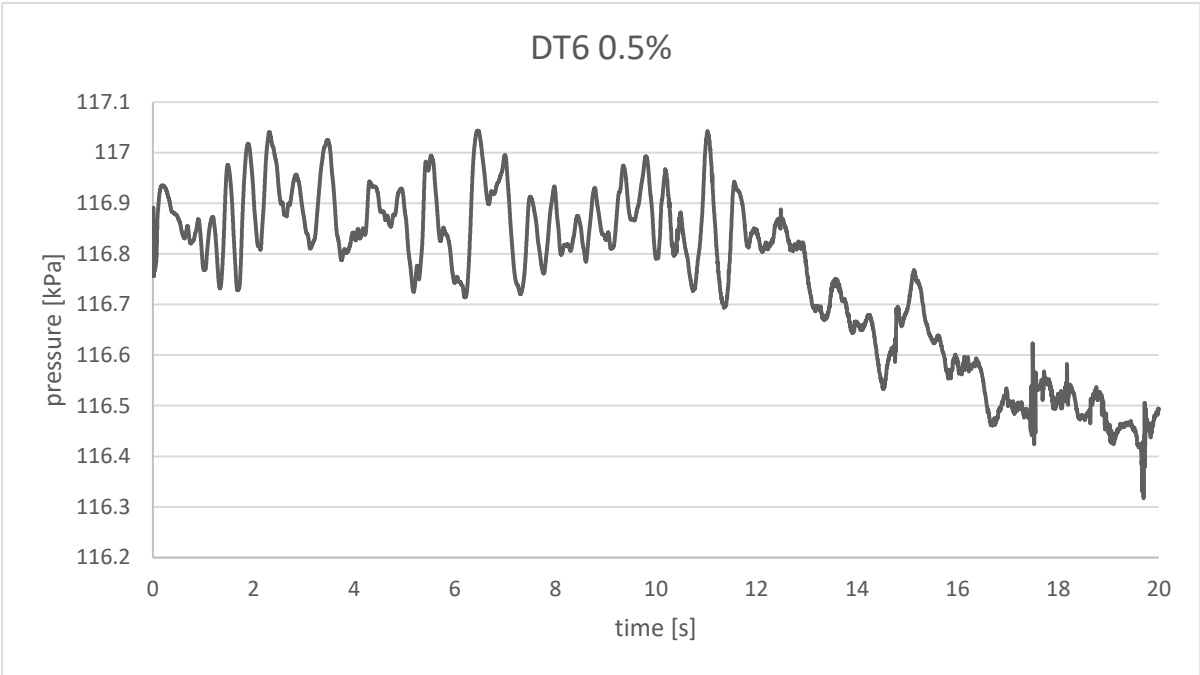
[31] A. Minakov, D. Platonov, A. Sentyabov and A. Gavrilov, "Francis-99 turbine numerical flow simulation of steady state operation using RANS and RANS/LES turbulence model," in *Francis 99, Second workshop*, Trondheim, 2016.

[32] L. Pitorac, D.-M. Bucur and M. Cervantes, *Numerical Simulation of Maximum Pressure in Pipes during Expulsion of Entrapped Air,* Bucharest: Politehnica University of Bucharest, 2015.

[33] B. Indraratna, R. Pathegama, J. Price and W. Gale, "Two-Phase (Air and Water) Flow through Rock Joints: Analytical and Experimental Study," *ournal of Geotechnical and Geoenvironmental Engineering ,* vol. 10, no. 129, 2003.

[34] E. Stenmark, *On Multiphase Flow Models in ANSYS CFD Software,* Goteborg: Department of Applied Mechanics, Chalmers University of Technology, 2013.

[35] *ANSYS CFX Modeling Guide.*

[36] *ANSYS ICEM CFD User's manual.*

[37] "Francis 99 workshop webpage," [Online]. Available: https://www.ntnu.edu/nvks/francis-99.

[38] S. Wilhelm, G. Balarac, O. Metais and C. Segoufin, "Analysis of Head Loss in a Turbine Draft Tube by Means of 3D Unsteady Simulations," *Flow Turbulence Combust,* vol. 97, pp. 1255-1280, 2016.
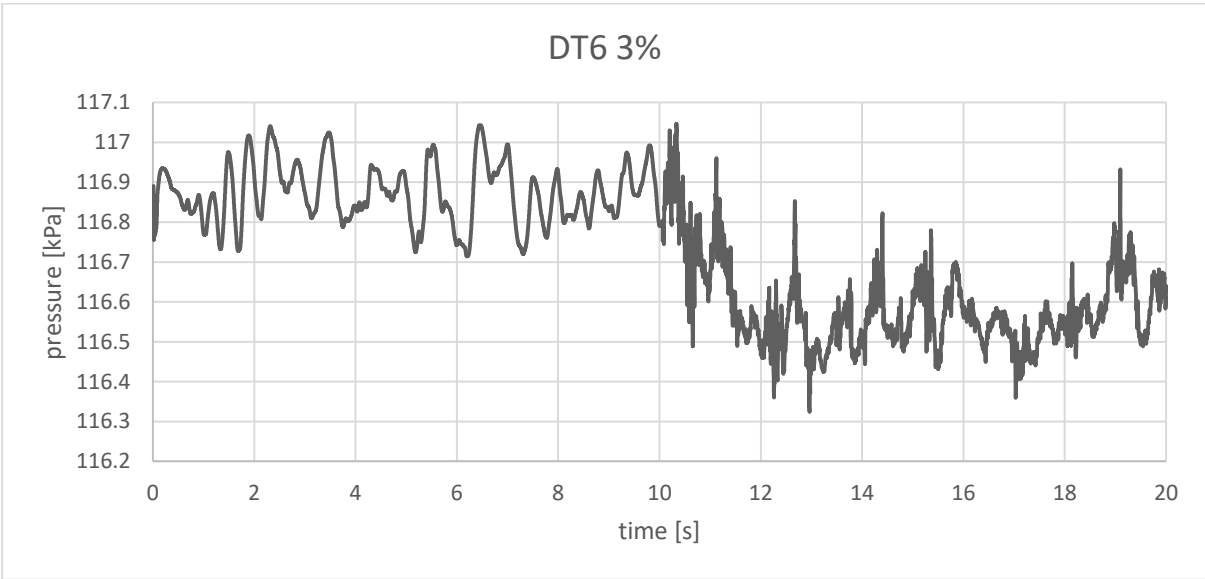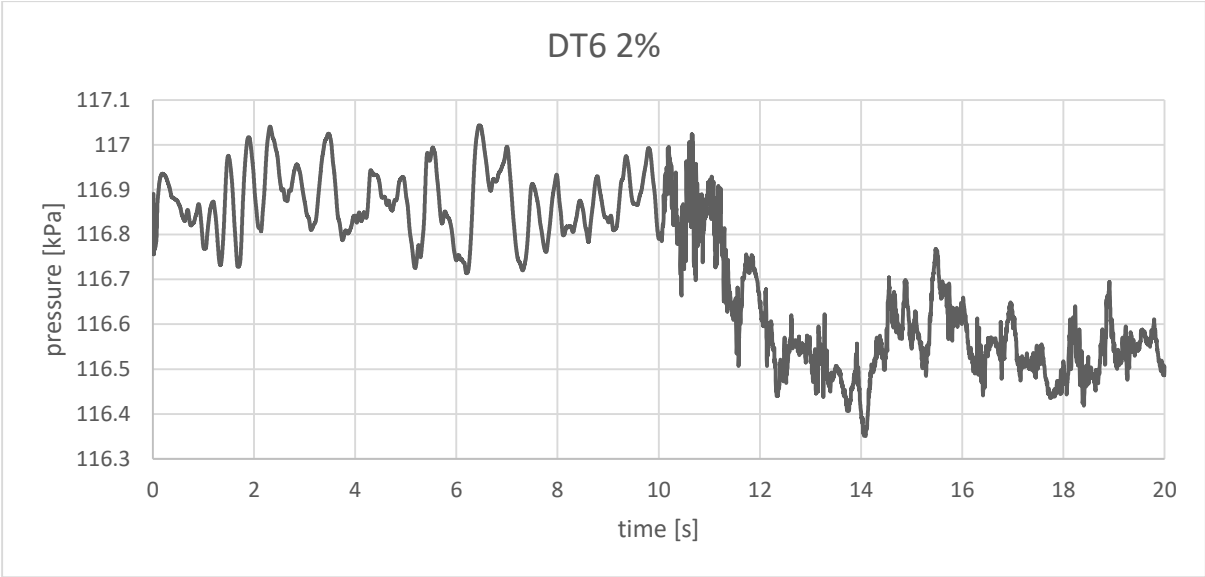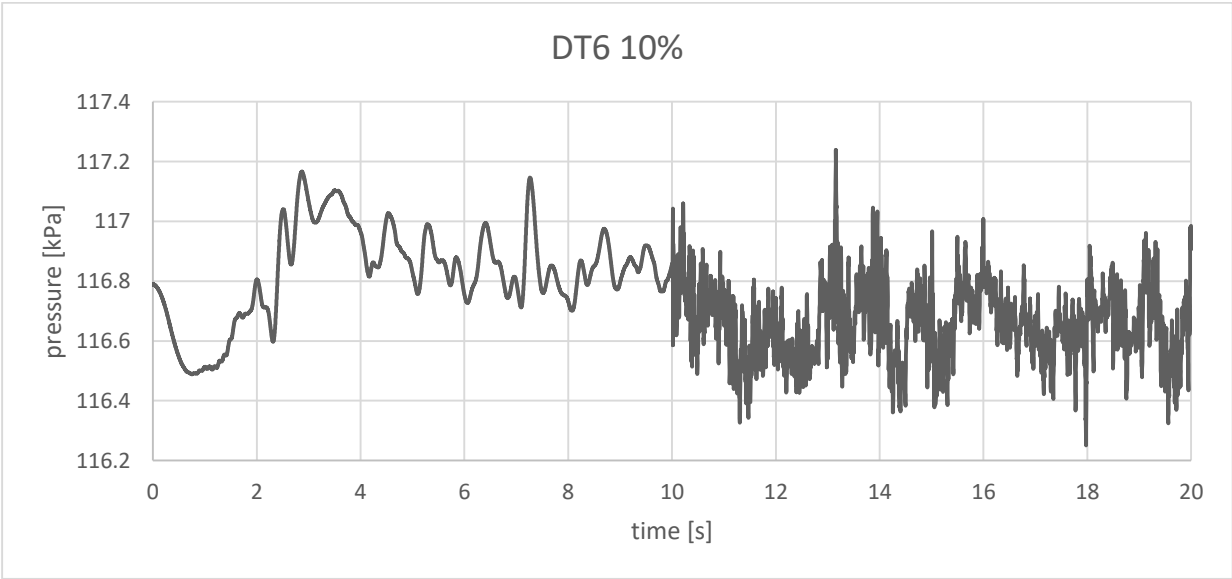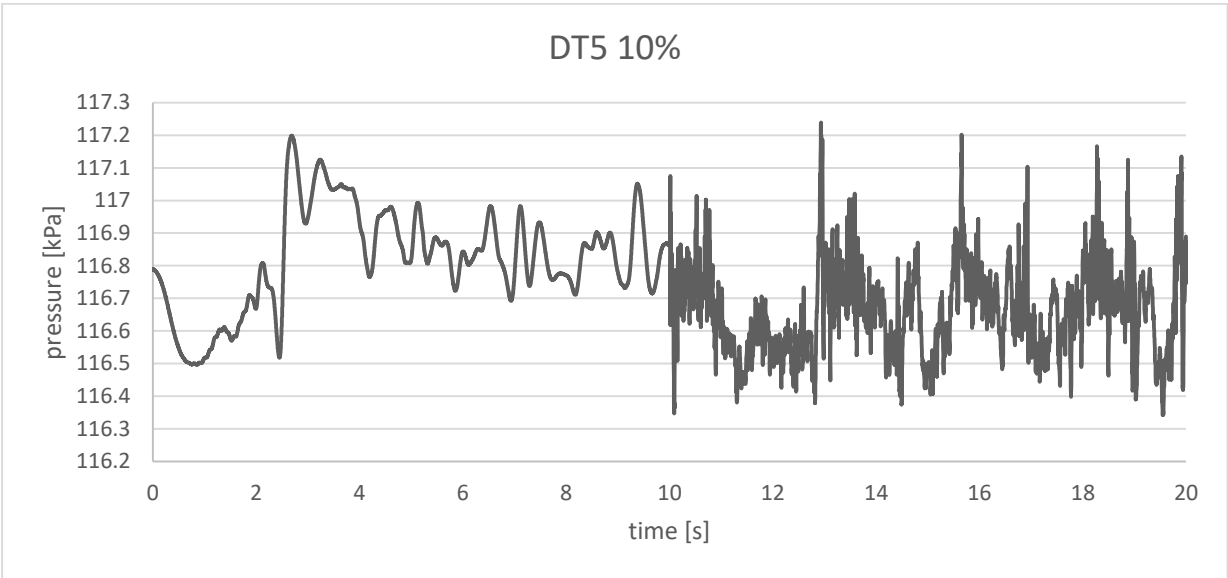
Appendix A

DT5 0.5%

DT5 1%

DT5 2%

DT5 3%

Appendix B

DT6 2%

DT6 3%

Appendix C

Appendix D

0.5%

2%

3%